Optimization of the neutron yield IN TU/e FUSOR

Huisman, A.E.

Award date:
2017

Eindhoven University of Technology
Department of Science and Technology of Nuclear Fusion
Department of Elementary Processes in Gas Discharges

Optimization of the neutron yield in TU/e FUSOR

A.E. Huisman

August 2017

Under supervision of:
R.J.E. Jaspers (TU/e, Fusion)
A. Sobota (TU/e, EPG)

Abstract

Experiments were performed on the TU/e Fusor, a gridded inertial electrostatic confinement (IEC) fusion reactor, with the purpose of maximizing the neutron production rate (NPR) using the $D(d,n)^3He$ reaction. Beneficial effects of optimizing the ion energy distribution were investigated, as well as the effects of utilizing fusion with D-nuclei embedded in a Titanium target.

Compared to a general star-mode discharge, the population of fast ions was increased by injecting ions directly at the peak potential of the fusor using an edge-mounted ion source. The effects were monitored by spectroscopy, which qualitatively confirmed an increase in the fast ion population. Obtained neutron rates were compared to a simple physical model which allowed a basic NPR scaling law specific to the TU/e fusor to be derived. While no direct correlation between neutron production rate and the increase of the fast ion population could be demonstrated, the ion source was shown to have a stabilizing effect on the discharge, allowing more extreme discharge powers. A resulting maximum neutron production rate of $(1.43 \pm 0.14)*10^6$ neutrons/s was measured, which embodied a factor 3.5 improvement over the best unassisted star-mode discharge in the same experimental configuration. Based on these findings, a novel fusor design is proposed which is expected to significantly increase the neutron yield.

Benefits of fusion with D-implanted Ti were investigated through comparison between non-implanted and D-implanted Ti samples suspended in the fusor. A maximum increase in NPR of 40% between these samples was demonstrated for low production rates, while the resulting total NPR was lower than a comparable discharge without a target. Fusion with D-implanted Ti targets was concluded to be impractical in a fusor. Non-intrusive applications of embedded fusion are discussed.

Acknowledgements

During my project on the TU/e Fusor, a good amount of people contributed in their unique ways to the successful completion of my master project. To these people, I would like to extend my sincere gratitude.

First of all, I would like to thank my supervisors Roger Jaspers (Nuclear Fusion) and Ana Sobota (Elementary Gas Discharges) for their continued scientific guidance and the fruitful scientific discussions along the way. I would also like to thank Hans Oosterbeek, for taking the time to teach me how to safely operate the fusor with regards to high-voltage operation and radiation safety. Furthermore I would like to mention Mark Verbeek and Mark Scheffer for their continued support with regards to the fusor's control-hardware *and* software.

Special thanks goes out to Herman de Jong (who was present during all experiments) for his practical guidance with regards to changing the experimental setup, and for being the walking encyclopedia that can give a (very) thorough answer to any scientific question faster than Google.

Table of contents

1 Introduction and research questions

1.1 Fusion

Nuclear fusion has been a hot (150 million K) topic of research and discussion since its theoretical discovery in the 1920's, as Sir Arthur Eddington theorized light nuclei fusing together in the sun release large amounts of energy [1]. Ever since the early 50's, attempts were made to develop schemes for harvesting this energy on earth. Still under continuous development, the largest experimental fusion reactor is currently being built in Cadarache, France. This device, ITER, aims to demonstrate the viability of harvesting net power gain from nuclear fusion by confining a hot plasma into a donut-shaped vessel called a tokamak [2]. Currently, tokamaks and its derivatives (stellarators, spheromaks) are closest to achieving the conditions required to produce surplus energy through thermonuclear fusion on a commercially viable scale.

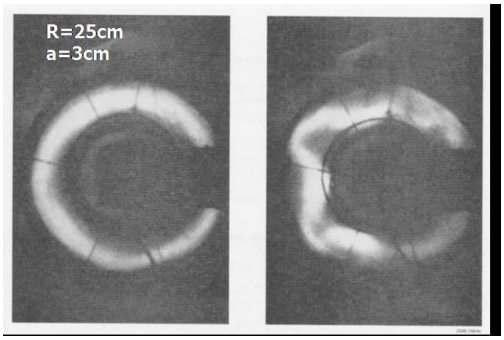

Figure 1: Early image of a toroidal pinch, used in early attempts to confine a plasma to achieve nuclear fusion. The right panel shows the plasma experiencing a kink instability.

All proposals for achieving nuclear fusion since the early 50's have one thing in common: plasma needs to be confined. Over the years, a multitude of different configurations have been proposed, tested and evolved from, such as the simple magnetic pinch (Figure 1). The vast majority of these proposals proved to be incapable of producing net energy or were increasingly difficult to stabilize. Eventually the route to fusion evolved into the mainstream approaches of today: tokamaks, stellarators and spheromaks. Along this route a legacy of devices was left behind that could not break-even in terms of energy production. This does not mean these devices do not *work* in terms of fusion occurring. Especially compact configurations can be of value as a neutron-source. One of such configuration is based on inertial electrostatic confinement (IEC): the Fusor.

1.2 The Fusor

The Farnsworth-Hirsch Fusor, named after its designers, is a table-top sized device that accelerates ions toward a central region by means of a strong (~250kV/m) concentric static electric field. Oscillating through this central region, the fast ions fuse upon collision with either background gas or another fast ion. This mechanism was soon demonstrated by the detection of high-energy neutrons [3].

While the Farnsworth-Hirsch fusor has existed for over 50 years, still little is known about the exact plasma behavior inside the reactor, as its low density operation ($n \sim 10^{15}$ cm^{-3}) makes it difficult to characterize the plasma through common plasma-diagnostics such as Thomson-scattering and plasma-oscillation based techniques. Additionally, interest of the scientific community faded when fusors proved incapable of producing surplus energy due to radiation and collision losses inherently overshadowing energy gained from fusion reactions.

However, as the fusor is a simple and easily constructed tabletop design, it remains a popular choice in both casual enthusiast endeavors as well as professional applications where a compact neutron source is required. As fusors were mostly abandoned, a lot of room for optimization remains. While disqualified for energy production, a strongly optimized fusor could be used in commercial applications, as well as for medical research through production of radioisotopes [4]. Currently fission reactors are used to produce adequate neutron fluxes for most commercial processes, while a fusor requires an increase in neutron yield by several orders of magnitude to compete.

1.3 Research questions

In this thesis, an attempt is made to optimize the TU/e fusor, currently producing ~$5*10^6$ neutrons/s, to compete with other IEC based neutron sources which routinely achieve 10^8 neutrons/s [5]. A target neutron rate of ~10^9 s^{-1} is set in an attempt to beat the competition for D-D IEC based fusion. Two possible avenues of improvement are investigated by seeking to answers to the following research questions:

1) Can the fraction of fast ions in the ion energy distribution of a fusor-discharge be maximized in order to maximize the neutron yield?

2) Will significantly increasing the number density of D in the center of a fusor – by means of installing solid deuterium-loaded target-material inside the fusor – provide a significant increase in neutron yield compared to a conventional discharge?

3) Can neutron yields of 10^9 s^{-1} be achieved by fully utilizing these optimizations?

First, an attempt is made to increase the fraction of fast (>50keV) ions inside the fusor-discharge by using a direct ion source, as most ions are expected to be significantly slower than the fusor ideally allows (see section 2.3.1). Secondly, experiments with a solid deuterium-loaded target will be conducted as this would significantly increase the number density of D in the center of the fusor, which could help increase the neutron yield (see section 2.3.2).

2 Theory

2.1 Nuclear fusion

To understand the research presented in this paper, a short introduction to the basics of nuclear fusion is required. In this section, the main reaction mechanisms as well as the factors that influence the total efficiency of fusion reactions and processes are discussed.

2.1.1 D-T / DD fusion

The principle of nuclear fusion is similar to fission, in the sense that a reaction occurs that results in an element with a higher average binding energy. The surplus of this binding energy is released in the process in the form of high-energy fast particles and radiation. In principle, almost all elements lighter than iron can be fused for energy gain (see Figure 2), however only few are viable in a laboratory setup (as will be detailed in section 2.1.2). Fusing D (deuterium, also denoted H^2) and T (tritium, also denoted H^3) to create He^4 and a neutron is easiest, followed closely by D-D fusion [6].

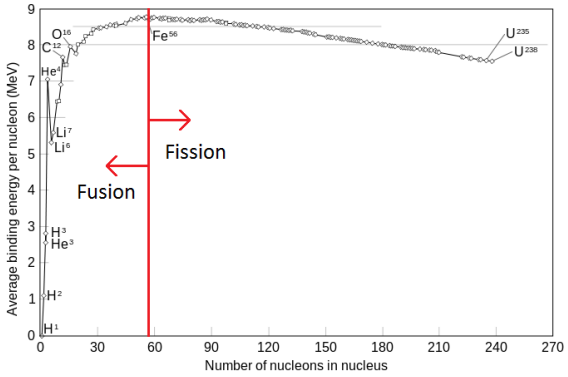

Figure 2: Average binding energy per nucleon as a function of the total number of nucleons in an element. As shown in the graph, Fe is the most densely packed nucleus, where lighter elements can be fused and heavier elements can be split in order to gain from this discrepancy in binding energy.

The reactions for D-T and D-D fusion are shown below.

D-D fusion: $${}^2_1D + {}^2_1D \rightarrow {}^3_2He + {}^1_0n + 3.27MeV\ (50\%\ probability)$$

$${}^2_1D + {}^2_1D \rightarrow {}^3_1T + {}^1_1H + 4.03MeV\ (50\%\ probability)$$

D-T fusion: $${}^2_1D + {}^3_1T \rightarrow {}^4_2He + {}^1_0n + 17.59MeV$$

Evidently, D-T gives a lot more energy per reaction than D-D fusion. In terms of energy production, D-T fusion is the most favorable for reactor-scale fusion such as ITER. However, since tritium is scarce (expensive) and radioactive, laboratory setups generally employ the D-D reaction as D is abundantly available while the process is still similar to D-T fusion. For these reasons, the fusor is also operated using only deuterium.

2.1.2 Cross sections and reaction rate

Similar to fission, fusion does not occur naturally on earth, as it is not a spontaneous process. Nuclei need to be pressed together, and since fusion is a process between ionized particles, the Coulomb force of two repelling positively charged nuclei needs to be overcome. Fusion only occurs naturally in stars, where conditions are extreme enough due to gravitational pressure. In a laboratory setting the nuclei need to be accelerated towards each other artificially. Furthermore, an optimal resonant interaction energy between nuclei needs to be found. No fusion occurs at low energy, while at exceedingly high energy the probability for fusing decreases with respect to the resonant maximum. This probability for fusion to occur at a specific ion energy is expressed numerically as a 'cross-section' (σ) in m^{-3}, which draws a parallel to rigid-body collisions where bigger particles with a larger physical cross-sectional area have a higher chance of colliding. In fusion, however, nuclear quantum-mechanical effects yield an energy-dependent cross-section with a resonant peak, as shown in Figure 3 for various fusion reactions.

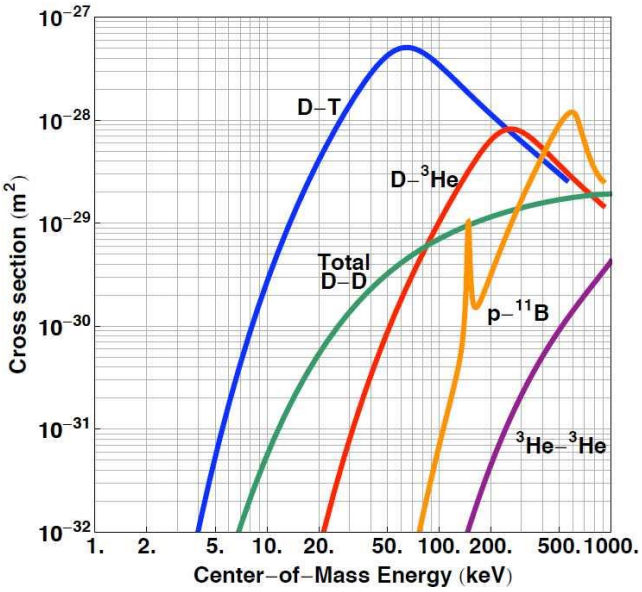

Figure 3: Fusion cross-sections for several fusion processes. D-T is the easiest, followed by D-D. Higher energy generally yields a higher cross-section.

From Figure 3 it is evident that D-T is the easiest fusion reaction to pursue in the lab, as it has the highest cross-section at the lowest energy. For D-D fusion, considerably higher ion energies are required.

In terms of these cross-sections, energy gain from fusion seemed impossible as the cross-section for coulomb collisions is higher than the fusion cross-section. This means that for nuclei accelerated towards each other, most energy will be lost as particles are more likely to scatter away instead of fusing. To overcome this problem, all reactor designs have one thing in common: there needs to be a confinement mechanism that ensures energetic ions remain inside the plasma. In large projects such as ITER, ions are confined magnetically, where the resulting gyrokinetics keep these ions mostly confined along the magnetic field lines. With the plasma and the magnetic field-lines shaped into a torus, transport radially outwards is inhibited (to a certain extent), providing the confinement mechanism. An older approach, mostly abandoned in terms of commercial energy production, is inertial electrostatic confinement (IEC).

2.1.3 Inertial Electrostatic Confinement (IEC)

Instead of a toroidal magnetic configuration, a static concentric electric field creating a concentric potential well can be used to confine a plasma and keep fast ions from escaping. With appropriately chosen anode/cathode structures, the ions are made to oscillate inside this potential well and are as such recirculated until fusion occurs (or until the energy is lost through another mechanism). Usually two concentric grids are used to create the field, the inner grid being of high transparency in order to allow the ions to pass through. Such setup is called a 'fusor', derived from the original Farnsworth concept [7]. Alternative IEC designs, like the Polywell [8], try to utilize virtual potential structures such that grid-losses can be avoided. While the field is static in IEC configurations, the system is dynamic due to the oscillatory motion of the ions, hence 'inertial'.

The most important loss mechanisms in gridded devices are:

- Bremsstrahlung from rapid acceleration and deceleration of plasma species
- Charge-exchanges losses where a fast ion exchanges an electron with a slow neutral, meaning the fast particle is no longer confined and lost to the wall
- Grid-losses, since the cathode grid can never be 100% transparent

For these reasons, electrostatic confinement has been abandoned as a viable energy reactor, as it is currently about 5 orders of magnitude short of reaching break-even [5]. As mentioned, IEC can still be utilized as a strong neutron source. The simplicity of its small physical design (~1 meter in diameter) and the ability to easily switch it on on/off make it a strong contender against the currently used fission reactors, which has obvious drawbacks in terms of start-up time, control, size and radiation/waste. This design simplicity doubles as its main weakness, however. Due to the spherical nature of the device and the resulting electric field, certain key plasma parameters are far from optimized for a D-D fusion process, as will be discussed in the next section.

2.2 TU/e FUSOR

In particular and shown in Figure 4, the IEC configuration used in this research is called the TU/e Fusor. Created in the image of the original Farnsworth concept, it uses a concentric electric field created between two physical electrodes to accelerate ions towards the central region, where collisions between ions or ions and neutrals yield fusion reactions. At high field strength (achieved by reactor voltages of in practice ~60 kV) and appropriate pressure, the ion density and D-D reaction rate are high enough to produce ~10^7 neutrons per second. Similar rates have been observed in other gridded devices [9].

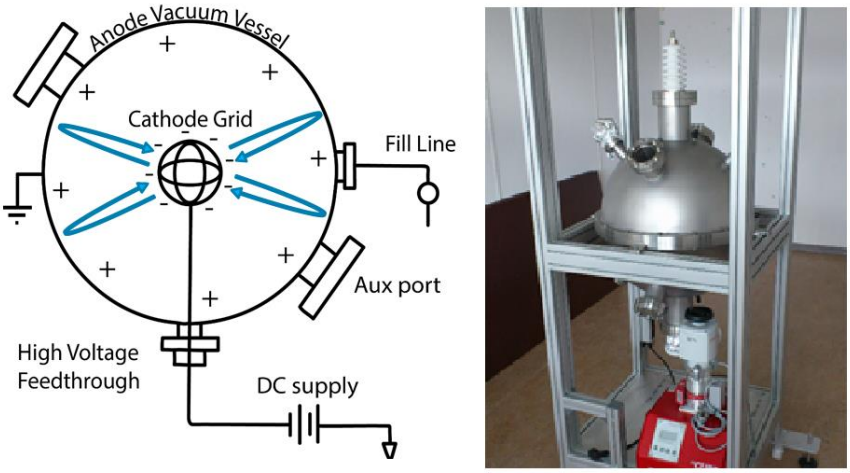

Figure 4: Simple schematic of the TU/e FUSOR on the left, bare setup without peripherals on the right. The central grid is connected to a power supply and creates a concentric electric field between the outer shell (grounded anode) and center grid (cathode). Schematic courtesy of A.J. Wolf [10].

The exact configuration of the TU/e Fusor will be discussed in the experimental setup (section 3.1). This section is intended to discuss some relevant theory regarding the fusor as IEC-device specifically.

2.2.1 Fusor potential and electric field

Since a Fusor acts as a spherical particle accelerator, it is important to understand the shape and potential inside. As the anode is grounded, and the cathode (grid) is held at a set potential V_0, solving the Laplace equation $\nabla^2 V = 0$ in spherical coordinates will yield the vacuum potential between the two concentric shells with radius R_0 (grid) and R_1 (shell), assuming the space charge $\rho = 0$ between the anode and cathode. Choosing a general solution in the form $V(r) = \frac{c_1}{r} + c_2$ which satisfies the Laplace equation with boundary conditions $V(0) = V_0$ and $V(R_1) = 0$, the resulting fusor potential is

$$(r) = -\frac{R_1 V_0}{\left(1 - \frac{R_1}{R_0}\right)}\frac{1}{r} + \frac{V_0}{\left(1 - \frac{R_1}{R_0}\right)} \tag{1}$$

which reduces to

$$V(r) = \frac{R_0 V_0}{(R_0 - R_1)}\left(1 - \frac{R_1}{r}\right), \qquad R_0 < r < R_1 \tag{2}$$

The electric field inside the fusor is now easily calculated through $\vec{E}(r) = -\nabla V$, yielding

$$\vec{E}(r) = -\frac{R_0 R_1 V_0}{(R_0 - R_1)}\frac{1}{r^2}\vec{e}_r, \qquad R_0 < r < R_1 \tag{3}$$

The resulting vacuum electric field and potential are plotted in Figure 5

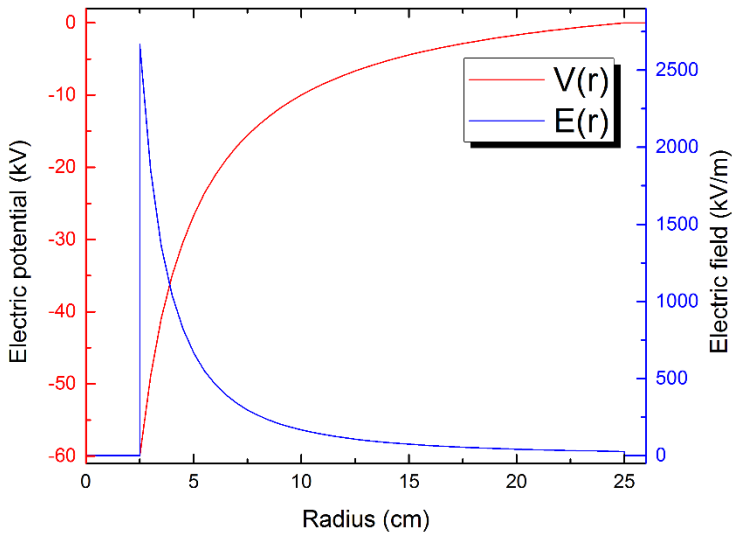

Figure 5: Radial electric potential (red) and field (blue) between cathode and anode for a Ø5cm cathode grid, for a fusor potential of -60kV. Due to the spherical concentric design of the electrodes, the electric field and potential are strongest near the grid.

Figure 5 shows that due to the spherical geometry of the concentric electrodes the electric field is stronger near the grid by several orders of magnitude compared to $r = 25cm$. This has important implications on the ion energy distribution – as a result of these field-shapes, electron-impact ionization of the background gas will occur mostly close to the grid, where the ions will only be able to experience a fraction of the maximum potential drop of 60kV. This will be further discussed in section 2.3.1.

2.2.2 Fusor specific discharge modes

In this thesis some recurring fusor-specific terminology will be used to describe the nature of the discharge, which will be introduced here. While it is not directly relevant to this research to have an in-depth understanding of these phenomena, it is useful for a reader to be familiar with these terms.

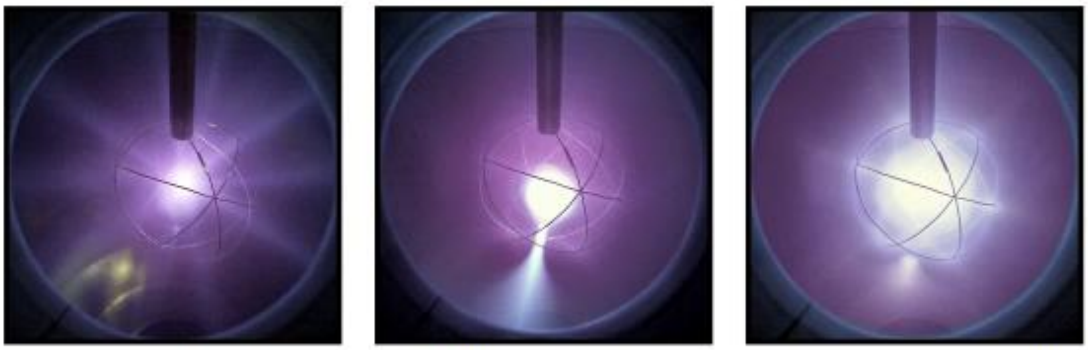

Figure 6: Various discharge modes observed in the TU/e Fusor. Different discharge modes are observed as the pressure is increased.

Fusor specific discharge modes (see Figure 6, [10]):

- Glow-mode: typically occurs at fusor pressure higher than several Pa. A glowing ball of plasma inside the fusor grid can be seen
- Jet-mode: occurs at moderate fusor pressure, between 0.5 and several Pa. A 'jet' can be observed exiting the central plasma, typically through the biggest hole in the cathode grid.
- Star-mode: occurs at low fusor pressure <0.5 Pa. Well defined beams or 'streamers' can be observed, giving the plasma a star-like shape. The streamers are believed to be the naturally occurring channels of oscillation for the ions.

The transition point between these modes differs per fusor configuration.

2.3 FUSOR optimization

As mentioned, the simplicity of the gridded fusor design leaves a lot to be optimized. Proposed optimizations and their justifications are discussed below.

2.3.1 Ion energy distribution

In a fusor, the main goal is to accelerate ions to the center as fast as possible, since the fusion cross-section scales strongly with the ion energy (see Figure 3 in section 2.1.1). However, it is assumed that during normal star-mode operation the ion energy distribution inside the fusor grid will behave like the sketch shown in Figure 7. This sketch indicates that given a discharge voltage of V_d, most ions will carry kinetic energies much lower than $E_{kin} = eV_d$. The reasoning behind this sketch is detailed below.

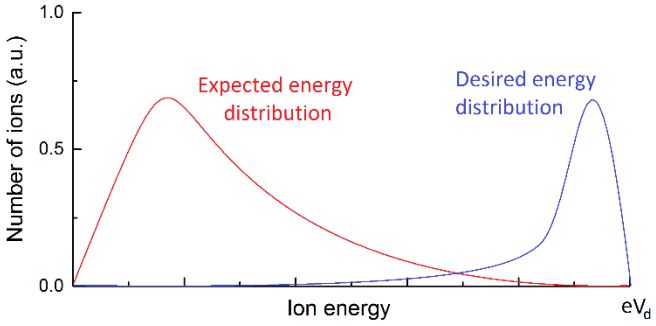

Figure 7: Expected (red) vs desired (blue) energy distribution in a typical FUSOR.

A fusor operates in vacuum at typical pressures of 0.15 Pa and below. As a result, the electron-ionization mean-free-path is generally much longer than the vessel ($\lambda_{mfp} \sim \mathcal{O}(10\ m)$ for H_2) such that electron avalanche no longer drives plasma breakdown. Instead of that, at sufficiently high electric field strength, field-emission from the grid gives enough free electrons for breakdown and sustaining the discharge. This acts as an extension on the left of the Paschen curve, which otherwise predicts an infinite required voltage [11]. Similarly, as the grid heats, thermionic emission further stimulates the creation of free electrons at the grid.

Since all electrons originate from the grid (secondary electrons freed from ionizations are neglected due to the long λ_{mfp}), the resulting ion energy distribution contains mostly slow ions due to the velocity-dependency of the electron-impact ionization cross section. This cross-section decreases rapidly for fast electrons, and since the electrons are only 'slow' near the grid, the probability of ionization will be significantly higher in that region. For example, from its maximum at 80 eV, an electron accelerated to 2000 eV has its ionization cross-section is reduced by factor 10 [12].

The majority of the ions are thus created in a region where they will only be able to pick up a fraction of the full fusor potential before reaching the cathode grid.

An attempt will be made to increase the fraction of fast ions by injecting D^+ directly at the edge of the vessel with a purpose-built ion source (see section 3.1.3). Contrasting star-mode operation, all the injected ions will be accelerated by the full fusor potential, and are thus expected to have a considerably higher fusion cross-section. The changes in the ion energy distribution will be investigated using spectroscopy (see section 3.2). The results of this are presented in section 4.1.

2.3.2 Embedded fusion

The second optimization is based on increasing the number density of deuterium in the volume inside the grid (at $r < 0.025$ m). In a fusor, interactions between ions and the background gas are believed to be the main driving mechanism for fusion, instead of direct D-D ion collisions [5]. The fusion yield then scales as

$$Fusion\ yield \sim n_i n_g \langle \sigma v \rangle \sim I \cdot p \cdot \langle \sigma v \rangle \tag{4}$$

An obvious way to increase the fusion yield would be to simply increase the pressure – more particles in the center of the machine would yield more collisions, and thus more fusion. However, increasing the pressure proves to be detrimental to the fusion yield for other reasons, as will be shown in section 4.1.3.

Additionally, if the pressure is increased further such that the mean-fee-path becomes shorter than the wall-to-grid distance inside the fusor, the ions would on average collide before being accelerated to fusion-relevant energies.

Therefore an attempt is made to utilize 'embedded fusion', where fast deuterium ions collide and fuse with D embedded in a solid material, such as titanium. This way the number density of D in the center of the vessel can be increased without increasing the vessel pressure. Constant trapping efficiencies of >90% were reported for D^+ implanted in Titanium at ion energies between 3.3 - 30 keV/H^+ [13]. Another study investigating the low-energy trapping coefficient for H^+ showed trapping efficiencies >60% for ion energies of 0.8 keV/H^+ [14]. Similar trapping coefficients were reported for deuterium implantation [15]. It is assumed that D^+ trapping mechanisms are similar and thus provide good trapping characteristics above ion energies of 1 keV/D^+. Additionally, as reflected D^+ is recycled by the spherical fusor potential, this reflected D^+ will strike the target again, increasing the effective trapping coefficient.

Another study has shown that loading Ti at implantation energies of 3.3 keV/D^+ for a total a fluence of 10^{17} D/cm^2 results in a deuterium-implanted region of 100 nm thick in the sub-surface of Ti, with a deuterium density of 0.2 D/Ti atoms [16]. For a surface area of 14 cm^2, this results in a total amount of $1.6*10^{18}$ D stored at the surface of the target. Even higher fluences result in loaded sub-surfaces of up to 500 nm thickness with a 1.0 D/Ti ratio, e.g. $4.0*10^{19}$ D. Compared to D_2 gas at background pressure of 0.15 Pa, which holds a total number of $9.45*10^{16}$ D_2 within a sphere (within the grid) of *r=2.5* cm, this gives over two orders of magnitude more D.

However, thermal desorption spectra of deuterium in titanium-deuteride films show thermal decomposition starts at temperatures of ~350 K and peaks at ~670 K for a TiD_2 film thickness of 100 nm [17]. To retain the embedded deuterium, the temperature of the target should be kept below these values to avoid outgassing. Moreover, rapid outgassing of the target introduces unwanted instabilities in the background pressure, which should also be avoided. As such, experimental settings (in terms of voltage and current) need to be moderated when a significantly increased target temperature is observed.

2.3.3 Simple fusor scaling-model for predicting neutron yield

A simple fusor model can be constructed 'back of the envelope'-style, in order to compare the neutron yields obtained in this thesis to the scaling that is expected on basic physical grounds. Some assumptions are made and some factors omitted – these will be justified accordingly. The starting point for the simple scaling-model is the neutron yield for a collection of fast ions at some velocity v_{fast}, assuming the dominant fusion mechanism is ion-neutral interaction (ions colliding with background gas) [5]:

$$Neutron\ yield = Volume * n_i n_g \sigma(keV) v_{fast} \tag{5}$$

In this case *σ(keV)* is defined as the cross-section for the D(d,n) reaction as a function of projectile energy. This is thus specifically the cross-section for the neutron branch (section 2.1.1) of D-D fusion between a stationary target and projectile deuteron with projectile energy in keV, contrasting the center-of-mass approach shown in Figure 3. For ease of use in this model, *σ(keV,CM)* is calculated using the R-matrix fusion cross-section parameterization as derived by Bosch et. al. [18]. The exact formula and used parameters can be found in Appendix B.

Assuming a single ion beam and assuming the fusor current scales directly to n_i, the discharge can be modeled as a single beam (which is reasonable, as a star-mode discharge manifests as multiple identical beams). This yields:

$$n_i = \frac{I_{fusor}}{e v_{fast} A_{beam}} \tag{6}$$

and

$$Volume = A_{beam} * d \tag{7}$$

where *d* is the diameter of the vessel (total length of the beam). The gas density n_g scales directly to the pressure via

$$n_g = \frac{p}{kT} \tag{8}$$

where p is the pressure in Pa, k the Boltzmann constant and T the temperature of the gas, assumed room-temperature (300K).

Combining formulae (5) through (8) yields

$$Neutron\ yield = A_{beam} * d * \frac{I_{fusor}}{ev_{fast}A_{beam}} * \frac{p}{kT}\sigma(keV, CM)v_{fast} \tag{9}$$

Note that in the fusor, the collision energy in keV in the center-of-mass frame equals 0.5*eV_{fusor} in units of kV. The cross-section is thus a function of 0.5*eV_{fusor}. Eliminating v_{fast} and A_{beam}, inserting the numerical values for k, T and d (0.5m), and adding a factor 10^{-3} to scale I_{fusor} to units of [mA], the resulting simple scaling-model becomes:

$$Yield[\frac{neutron}{s}] = 7.54 * 10^{35} * I_{fusor}[mA] * p[Pa] * \sigma\big(0.5 * eV_{fusor}[kV]\big) \tag{10}$$

In this model, ion recycling is omitted since it is unknown how many oscillations an ion makes before either being lost to charge-exchange with a slow neutral or being lost to the grid. Furthermore, it is assumed the projectile particles are mono-energetic, which in a realistic setting will not be the case. This assumption should lead to an over-estimation in cases where the average projectile energy (and thus effective average cross-section) is lower.

2.4 Spectroscopy: spectral line broadening

Since a significant part of the results are based on the analysis of Doppler-broadening in optical spectra, it is prudent to briefly discuss the (other) broadening mechanisms that occur during spectroscopy. Amongst these mechanisms are natural broadening, pressure broadening, Doppler-broadening and instrumental broadening. Stark broadening was briefly investigated as this can be significant in H-like plasmas, but proved to be negligible at the electron density expected in a fusor (~10^{15} m^{-3}) [19]. In this section it will be shown that only Doppler-broadening and instrumental broadening are relevant, since the remaining mechanisms are too minor at the low pressure to have an effect. For reference (see section 3.2.1), calibration results on a low-pressure argon lamp indicate a Gaussian broadening of $\mathcal{O}(0.1\ nm)$ / of order 0.1 nm.

The main purpose of spectroscopy in this experiment is to monitor, qualitatively, the energy distribution inside the fusor and to link this to fusion yield. Since singly charged ions can gain up to 60keV of kinetic energy from a 60kV fusor potential, very light elements such as hydrogen and deuterium are expected to show spectral Doppler shifts as large as several nm.

2.4.1 Natural linewidth broadening

Natural linewidth broadening is a result of quantum physics, and is caused by the fundamental uncertainty principle in excited states with short lifetimes. Formally, the uncertainty principle reads

$$\Delta E \Delta t \geq \hbar/_2 \tag{11}$$

which states that for an excited state with a short lifetime, the inherent uncertainty in the energy of this excited state is $\hbar/_{2\Delta t}$. For the Ballmer-α transition from $n = 3$ to $n = 2$ with a lifetime of ~10^{-8} s [20], the ΔE of an emitted photon then equals

$$\Delta E_{photon} = 2 * \hbar/_{2\Delta t} = 1.05 \cdot 10^{-26} Joule \tag{12}$$

which holds an additional factor two due to the uncertainty principle applying to both the $n = 3$ and $n = 2$ state. On the central wavelength of this transition (E_0 = 3.02 * 10^{-19} J for λ_o = 656.2 nm) the resulting total natural broadening is easily calculated through

$$\Delta\lambda_N = 2\frac{\Delta E_{photon}}{E_0}\lambda_0 \tag{13}$$

where E_o is the energy of the central wavelength λ_0. Note a factor 2 is added since the total broadening spans from $E_0 - \Delta E_{photon}$ to $E_0 + \Delta E_{photon}$. The resulting total broadening is $\Delta\lambda_N \approx 4.6*10^{-5}$ nm. Since $\Delta\lambda_N$ << 0.1 nm, this is considered a negligible effect.

2.4.2 Pressure broadening

Through influence of ambient neutrals, broadening and shifts can be introduced in the spectral lines of a plasma. Such broadening is called pressure-broadening, as it scales linearly with the neutral gas density. It is generally considered negligible for most plasmas [21]. Due to the scaling with n_g, pressure broadening is considered negligible in this thesis as a fusor plasma is operated at near-vacuum conditions (~0.1 Pa, $n_g \sim 10^{19}$ m^{-3}).

2.4.3 Doppler broadening and shifts

Doppler effects are of significant importance to this work. First, a distinction must be made between Doppler shifts and thermal Doppler broadening. While similar, both play a very different role in this work.

2.4.3.1 Thermal Doppler broadening

Thermal Doppler broadening is caused by the random thermal motion of particles in the plasma. A thermal distribution of hot particles can have significant average velocities inside a plasma, resulting in Doppler-shifted photons being emitted. Due to the thermal distribution these Doppler-shifted photons will show up in a spectrum as a broadened spectral line (Gaussian) around λ_0 of a specific transition. The width of this Gaussian is proportional to the average temperature of the plasma. Thermal Doppler broadening can be characterized by the following formula [21]:

$$\Delta\lambda_{FWHM}^{Doppler} = \lambda_0 \sqrt{8 \ln 2 \frac{k_B T}{mc^2}} \tag{14}$$

Since a fusor plasma is generally cold ($\mathcal{O}(1\ eV)$) this effect is expected to be small compared to the Doppler-shift of the oscillating fast fusor ions. However, depending on the quality of the spectrometer, it should be measurable since the thermal broadening $\Delta\lambda_{FWHM}^{Doppler} = \mathcal{O}(0.05\ nm)$ for a 1 eV plasma.

2.4.3.2 Doppler shift

The Doppler shift is expected to be of significant importance as the fusor accelerates ions to up to 60keV, which results in near-relativistic velocities for light ions such as H and D. Resulting Doppler shift of several nm are expected. The measured Doppler shift will be used to determine the corresponding kinetic energy of species that show distinct Doppler-shifted features in the spectra. A specific differentiation between Doppler shift and Doppler broadening is made, as "Doppler broadening" implies a perfectly symmetric Gaussian distribution around a central line, which – as the results will show – is no longer the case when a near-mono-energetic energy population is injected and measured. These will produce shifted and arbitrarily peaked functions next to the central line, their exact shape depending on the actual energy distribution of the injected particles.

The Doppler shift for individual particles is derived below. In this derivation it is assumed that the Doppler-shifted species of interest travel parallel to the line-of-sight of the spectrometer. This is justified by the geometry of the setup used in this thesis (see 3.2), where the spectrometer is positioned directly opposite to a particle source. Therefore directional coefficients are omitted in this derivation.

First, the Doppler shift in frequency for electromagnetic waves for a source moving away (redshift) from the observer is given by [22]:

$$f_{observed} = \sqrt{\frac{c - v}{c + v}} f_0 \tag{15}$$

Here, c is the speed of light, v the velocity of a radiating particle moving towards the observer, and f_0 the emitted frequency. Rewriting this formula in terms of λ instead of frequency yields:

$$\frac{\Delta\lambda}{\lambda_0} = \sqrt{\frac{c - v}{c + v}} - 1 = \sqrt{\frac{1 - \beta}{1 + \beta}} - 1 \tag{16}$$

where $\beta = v/c$. At low $\Delta\lambda$ formula (16) can be solved for v and substituted in $E_k = {}^1/_2\, mv^2$ to yield

$$E_k = \frac{1}{2} m \left(c \frac{((\Delta\lambda)^2 + 2\lambda_0 \Delta\lambda)}{(\Delta\lambda)^2 + 2\lambda_0 \Delta\lambda + 2{\lambda_0}^2} \right)^2 \tag{17}$$

Thus for given (measured) values of λ_0 and $\Delta\lambda$, the kinetic energy of an atom emitting a photon can be immediately calculated.

Since ions are expected to be accelerated to energies of up to 60keV (v < 0.01c), relativistic effects in calculating the kinetic energy can be neglected. For completeness, the relevant relativistic derivation is shown here anyway. The kinetic energy can be calculated by solving formula (16) for β and substituting in the formula for relativistic kinetic energy:

$$E_k = m\gamma c^2 - mc^2 = \frac{mc^2}{\sqrt{1-\beta^2}} - mc^2 \tag{18}$$

This yields

$$E_k = \frac{mc^2}{\sqrt{1-\left(\frac{((\Delta\lambda)^2 + 2\lambda_0\Delta\lambda)}{(\Delta\lambda)^2 + 2\lambda_0\Delta\lambda + 2{\lambda_0}^2}\right)^2}} - mc^2 \tag{19}$$

2.4.4 Instrumental broadening

Finally, instrumental broadening is broadening caused by the setup, and depends on the optics used and the settings at which the spectrometer is operated. For instance, using a wider slit entrance or a grating with lower line-density will result in a larger FWHM for an otherwise narrow emission line. To determine the instrumental broadening of the setup, a low pressure low temperature Ar lamp can be used such that collisional broadening and thermal Doppler broadening can be assumed negligible. What remains is the instrumental broadening of the setup. The calibration results for the spectrometer used in this thesis are shown and discussed in section 3.2.1.

2.4.5 Linewidth deconvolution

When a spectral line is broadened by multiple mechanisms, the linewidths of both mechanisms will convolute into a larger FWHM if their individual broadening is of similar magnitude. When the line-shape (Gaussian, Lorentzian, Voigt) of both broadening mechanisms and the line-width of at least one is known, the measured spectral line can be deconvoluted, yielding the FWHM of the broadening mechanism of interest. This way the contribution of the instrumental broadening can be removed from the measured spectral line.

For two individual Gaussian broadening mechanisms denoted *G1* and *G2*, the total FWHM $\Delta\lambda^G_{FWHM}$is determined by [21]:

$$(\Delta\lambda^G_{FWHM})^2 = (\Delta\lambda^{G1}_{FWHM})^2 + (\Delta\lambda^{G2}_{FWHM})^2 \tag{20}$$

As a result, when the instrumental broadening $\Delta\lambda^I_{FWHM}$is known, the Doppler broadening of a spectral line can be determined through:

$$\Delta\lambda^{Doppler}_{FWHM} = \sqrt{(\Delta\lambda^{total}_{FWHM})^2 - (\Delta\lambda^{Instr.}_{FWHM})^2} \tag{21}$$

For results where $\Delta\lambda^{total}_{FWHM} >> \Delta\lambda^{Instr.}_{FWHM}$, this correction can be ignored.

3 Experimental setup

3.1 TU/e Fusor

3.1.1 General

This fusor (see Figure 8) is a spherical metal vacuum vessel (R_1 = 25 cm) acting as anode with a spherical cathode grid in the center. The cathode grid is connected to a Heinzinger HNCs 120000-100 DC Cockcroft-Walton-type negative power supply capable of 100 mA and -120 kV. A ballast resistor stack of 210 kΩ is connected in-series with the fusor in order to stabilize the discharge and protect the PSU. Rigid copper tubing of Ø(1 cm) is used for the power line towards the fusor. Note that the ballast resistor introduces a voltage drop, such that the discharge voltage V_d differs from the set voltage V_0 by:

$$V_d = V_0 - IR \tag{22}$$

Vacuum pressures as low as 0.015 Pa are maintained by a Pfeiffer Vacuum HiCube vacuum pump assembly combined with a Pfeiffer Vacuum HiPace 80 1500Hz turbo pump. A pressure control-range of 0.03-10 Pa is maintained by a remotely operated stepper-motor valve (Pfeiffer Vacuum EVR 116) that allows the target gas (usually H_2 or D_2) to enter the vessel. Vacuum pressure is monitored with a Pfeiffer Vacuum IMR 265 Pirani-type pressure gauge. A Pfeiffer Vacuum RVC-300 controller is used both to monitor the vacuum pressure and to control the EVR 116 inlet valve. The pressure setpoint is adjusted externally by software controls. The RVC-300 adjusts the inlet valve to maintain the pressure setpoint by balancing gas influx with the outflux through the vacuum pump. Additionally, the vacuum pump is equipped with a manual valve (Pfeiffer Vacuum EVB 063 SA) that can be used to reduce the outflux to avoid unnecessarily wasting expensive source gases when higher vessel pressures are desired.

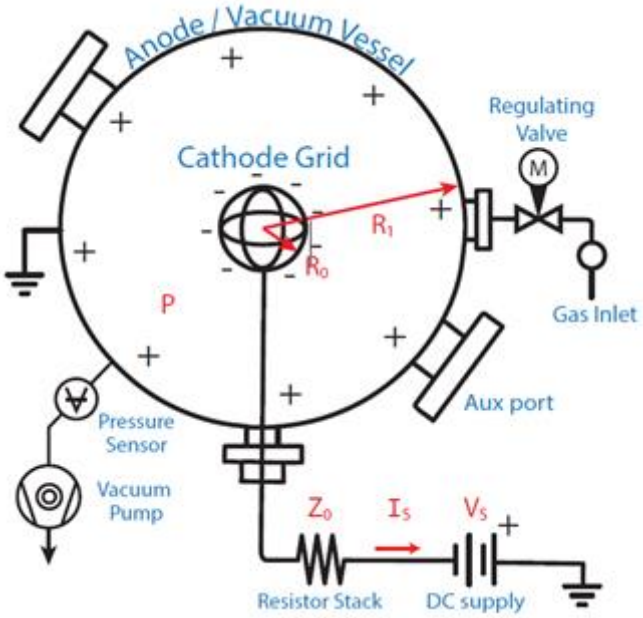

Figure 8: Schematic of TU/e Fusor including peripherals. Schematic courtesy of A.J. Wolf [10].

The grid is connected to the power-supply by a stainless steel rod via a ceramic high-voltage feed-through, which in turn is connected to the HV power-supply by a hollow copper rod. The stainless steel rod inside the fusor is insulated by a fused silica tube that fits tightly over the steel rod, to avoid the rod itself from actively participating in the plasma. Around the fusor, 4 sets of oppositely positioned auxiliary ports are mounted (two shown in the schematic) angled at 45º, which can be used for additional diagnostics.

The fusor is surrounded by neutron shielding (polyethylene) of ~10cm thickness to allow safe prolonged operation while inside the Fusor room. Additionally, a Studsvik 2202D neutron dosimeter is positioned directly outside the shielding to verify acceptable radiation levels during all deuterium operations.

3.1.2 Grid- and target-configurations

The fusor can be equipped with varying grid configurations. Originally, a Ø(10 cm) W grid with a wire diameter of 0.44 mm was installed in the fusor. For this thesis specifically, also a smaller Ø(6 cm) Ti grid with a wire diameter of 2.0 mm was constructed to investigate effects of embedded fusion. Additionally, a Ø(8.5 cm) icosahedron-shaped grid constructed out of Ti sheet mesh was constructed for similar experiments. These grids are shown in Figure 9.

Figure 9: Different grid configurations used in this thesis. From left to right: 1) W wire grid Ø 10 cm. 2) Ti wire grid Ø 6 cm. 3) Ti mesh grid Ø 8.5 cm.

To complement the deuterium loading experiments, a simple disk-shaped target was constructed. The target consists of a Ø(2 mm) Ti-wire coiled into a disk-shape and is suspended in the middle of the fusor grid (see Figure 10). The resulting surface area of a single side of the target is 6.7 cm^2. This target is then suspended inside the cathode grid, where it can be bombarded with ions by the ion source (see section 3.1.3) directly or by the star-mode plasma. Deuterium loading is performed inside the fusor at ~1 Pa and ~10kV discharge potential for 30 to 60 minutes. The total D-fluence of >1 keV/D^+ particles (required for embedding D in Ti, see section 2.3.2) can be roughly estimated by a back-of-the-envelope style calculation (see Appendix B) to be $\mathcal{O}(10^{18})$ D^+/cm^2, which should result in a deuterium loading of ~ 1 D/Ti in the first 100 nm of the target [16]. A V_d of 10 kV was chosen to make sure the bulk of the ions is above 1 keV/D^+, taking into account that D_2 may be a dominant population in the fusor plasma and the energy-distribution will not be mono-energetic (see section 2.2.1).

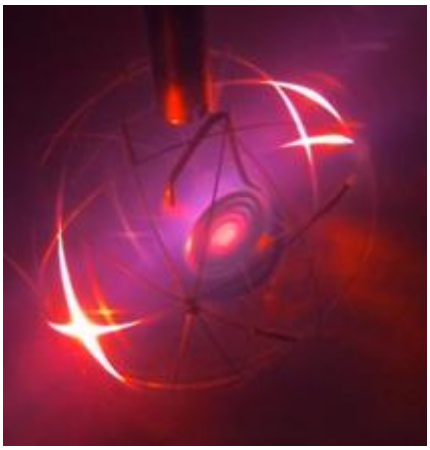

Figure 10: Titanium disk target constructed from of wound titanium wire, suspended inside the W wire-grid.

3.1.3 Ion source

For injecting deuterium ions at the edge of the vessel, a simple high-current ion source was constructed by the design of A. Seltzman [23]. A schematic of this source is shown in Figure 11. The ion source outer casing was constructed from ferritic stainless steel (type 410). The design utilizes a circular anode ring placed inside a cylindrical cathode, maintaining an adjustable gap of 1~2 mm. Rare earth SmCo magnets topped with a ferritic steel (type 410) pole piece are stacked over the central column for enhanced

ionization and appropriate ion beam focus. The sharp edge in the ion source casing stimulates field emission, allowing breakdown at relatively low voltage.

The anode is connected to a medium high-voltage (MHV) power supply with a maximum voltage of 5kV. In practice, the ion source is not operated at voltages higher than 2.5kV, with a maximum current of ~5 mA. The ion source is compatible with background pressures ranging from $1.3*10^{-2}$ Pa to 8.0 Pa [23].

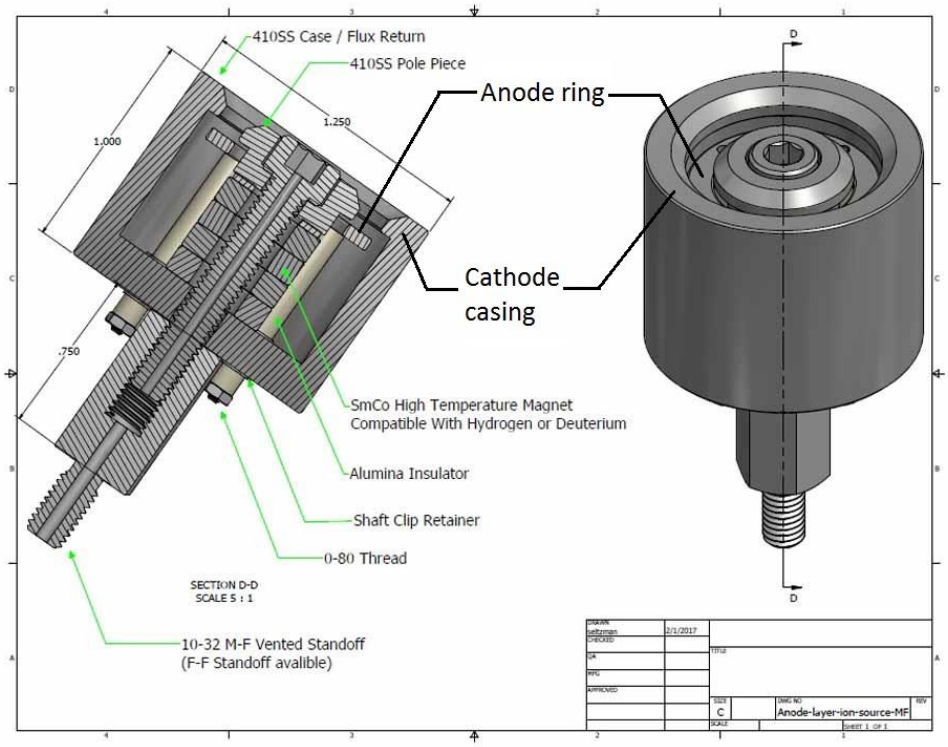

Figure 11: CAD diagram of anode layer ion source. Dimensions shown in the image are in inches. Design and image courtesy of A. Seltzman [23].

The source is installed in one of the bottom auxiliary ports of the TU/e Fusor. An auxiliary port flange was custom milled and fitted with appropriate gas- and HV-feedthroughs. The gas-feedthrough is equipped outside the fusor with a manual Pfeiffer Vacuum EVN-116 precision valve.

Since the ion source operates at medium high-voltage (several kV), the ejected ions will have a nonzero exit velocity. Depending on the operating voltage, this can be several keV. Ions then accelerated over the full discharge potential, will have surplus energy causing them to collide with the wall after a single passthrough. To avoid this, the ion source was driven by two separate power supplies (one for the anode, one for the cathode) in a floating (non-grounded) configuration. This way, the ion source can be biased as a whole. An offset was constructed that places the ion source slightly inside the concentric field. The source can then be biased to match the field potential, ensuring ions cannot reach energies in excess of $eV_{discharge}$.

3.2 Spectroscopy for monitoring ion energy distribution

To monitor the plasma through spectroscopy, an Andor Shamrock SR-500i spectrometer was used, coupled to a custom lens-system through a 400-2200 nm optical fiber. The lens stack was built and optimized on an optical table such that a ~ Ø 3cm column of parallel light is focused into the fiber entrance. This lens stack was then installed on the auxiliary port opposite of the ion source using a 45º mirror (as necessary due to lack of space, see Figure 12), so that the Doppler-shifted ions coming from the ion are parallel to the spectrometer line-of-sight, meaning no directional correction is required for the measurements of interest. For all spectra, a 1200 lines/mm grating was used with an entrance slit-width of 50 µm and accumulation time of 20 seconds per measurement.

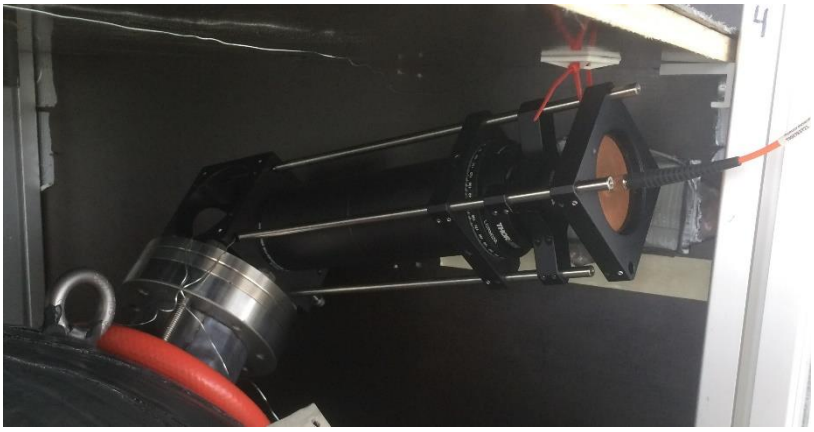

Figure 12: Mounting position of the spectrometer optics. The lens system was aligned on an optical table to optimize the light intensity coupled into the fiber from a parallel beam of light.

All measurements are performed on the Ballmer-α emission line for both H and D. The changes in the Doppler-shift profile around this peak can be used to qualitatively describe changes in the ion energy distribution inside the fusor.

3.2.1 Spectrometer calibration

For calibration of the wavelength axis, the internal calibration of the Andor SR-500i was used. This gives a reasonable calibration with a systematic error of ~0.5 nm. Since all analysis in this thesis will be performed based on relative differences in wavelength ($\Delta\lambda$) within the spectra, precise calibration of the wavelength-axis using an external light source was not required.

Appropriate spectrometer settings (slit width, accumulation time and grating setting) were obtained by performing trial measurements on a hydrogen test-plasma with the intention to find a balance between resolution (instrumental broadening) and signal strength. After trial and error, where the signal strength was increased as much as possible without saturating the spectrometer on the central peak of a spectral line, the spectrometer was set to use a 1200 lines/mm grating with a slit width of 50 μm. Accumulation time for each measurement is 20 seconds.

The instrumental broadening as determined by measuring the spectrum of an argon lamp positioned in front of the optical setup. The resulting spectrum is shown in Figure 32 of Appendix C. The shape of a spectral line is Gaussian with a FWHM of (0.12 ± 0.01) nm which is consistent over the three peaks shown. This is close to the maximum resolution of 0.06nm for the 1200 lines/mm grating as stated in the Andor SR-500i datasheet, and thus seems to be limited by the spectrometer hardware. Lowering the slit width did not improve the instrumental broadening.

Generally, when analyzing Doppler broadening mechanisms, it is customary to denote the total broadening of a spectral line (the full-width at half maximum, FWHM) as $\Delta\lambda$. However, due to the nature of the discharges analyzed in this thesis, the spectra are not expected to be perfectly symmetric. As such, when analyzing Doppler-*shifts*, $\Delta\lambda$ will be used to indicate the distance between the central line and a Doppler-shifted spectral feature. When a spectral feature is analyzed in terms of total FWHM, this will be designated specifically by $\Delta\lambda_{FWHM}$.

3.2.2 Considerations on analysis of spectra in a fusor

In a stationary plasma, analysis of spectra is relatively straight-forward as the broadening-mechanisms are generally well-defined, and can usually be fitted by known line-shape profiles (Gaussian, Lorentzian or Voigt). In a fusor, since the system is dynamic and both accelerating, decelerating and stationary species will be present in the line-of-sight of the spectrometer, a more arbitrary broadening shape is expected which is difficult to analyze in a 'classical' way. The oscillating ions are expected to dominate the broadening effects in the spectrum, since these will be travelling at ~60keV which should correspond to Doppler-shifts of up to 6 nm from the central line. However, the shape of the resulting broadening-profile is not expected to be simply a Gaussian. For a H_2 plasma, it is a result of a combination of the following factors acting simultaneously:

1) As stated in section 2.3.1, most ionizations are expected to happen near the grid, and as a result only a small fraction of H_2 is ionized at the edge of the vessel, meaning only a fraction of all plasma particles can be accelerated by the full potential.

2) As explained in section 3.2, spectroscopy is a line-of-sight measurement, meaning ions that undergo charge-exchange *outside* the center of the grid (where due to partial deceleration $v < v_{max}$) contribute as well.
3) Ions oscillating back-and-forth spend more *time* going 'slow' rather than going at maximum velocity in the center of the fusor. This increases the probability for charge-exchange to occur outside the grid when their velocity is well below the maximum. Additionally, the charge-exchange cross-section is velocity dependent [24].
4) Particles travelling diagonally or perpendicularly to the spectrometer line-of-sight will show a decreased Doppler-shift due to the observation angle, or simply no shift at all. Note that star-mode in the Fusor is not perfectly symmetric due to the electrode rod.
5) Both H^+ and H_2^+ are expected to be present in the plasma at unknown fractions, which – for the same ion energy – contribute to the spectrum at different values of $\Delta\lambda$ due to the difference in mass.

Since these factors can all contribute simultaneously in varying degrees, a 'classical' approach to analyzing the broadening shape will yield unsatisfactory results without first accurately modeling the fusor plasma, and fitting the convolution of the resulting theoretical distributions correlating with points 1-5. Such analysis is outside the scope of this thesis.

As will be shown in section 4.1.2, however, the addition of the ion source provides qualitative insights in the plasma composition since the source will inject ions that will in theory be accelerated to the same maximum energy. These ions, which in an ideal case reach the central grid with a near-mono-energetic energy distribution, should show up in the spectra as peaked features Doppler shifted from the central line. Convoluted with other broadening effects of other plasma populations, these mono-energetic populations can still be observed as transients in the overall broadening profile.

As discussed in section 2.3.1, an attempt will be made to increase the fraction of fast ions, by injecting D^+ directly at the edge of the vessel with a purpose-built ion source. This should be visible in the resulting spectrum as a higher photon count at higher $\Delta\lambda$ (Doppler-shift from the central 656nm emission line) compared to a regular star-mode discharge.

3.3 Monitoring neutron yield

For measuring the neutron yield, a Boron-Trifluoride (BF_3) neutron detector is used, specifically the Studsvik 5310C without the 2202D dosimeter, shown in Figure 13. This detector consists of a BF_3 filled proportional counter tube, surrounded by a moderator (polyethylene) to thermalize fast neutrons before entering the tube. The 5310C is connected to a Canberra HV Model 3005 HV power supply at 2.2 kV.

The resulting cps (counts per second) are measured over a prolonged period of time, and yields a neutron flux of (2.22 ± 0.15) neutrons $cm^{-2}\,s^{-1}$ per cps, given a neutron energy of 2.45 MeV as determined from the calibration curve in the Studsvik documentation [25]. It should be noted that the error of 0.15 is an unknown yet non-random systematical read-off error due to the precision of the calibration graph.

The detector is mounted in the default 90° configuration aside the fusor at a distance from the center of 48.7 cm from the center. The total flux surface at this radius is calculated via $4\pi r^2$, then multiplied by the obtained flux to yield the total fusor neutron yield in neutrons per second assuming an isotropic distribution of neutrons. Additionally fusion is assumed to occur mostly inside the grid, which is a reasonable assumption since ions by definition have maximum velocity inside the Ø6cm grid.

For a radius of 48.7 cm, the total flux surface is $2.98*10^4$ cm^2. Therefore the number of counts per seconds simply scale as:

$$\begin{aligned} Neutron\ yield &= cps * 2.22 * 2.98 \times 10^4 \\ &= (cps * 6.61 \times 10^4)\frac{neutrons}{s}\ (\pm 6.8\%\ systematical) \end{aligned} \tag{23}$$

where the 6.8% error is a systematical one caused by the uncertainty in the conversion factor obtained from the calibration graph. This error acts as an identical offset to every measurement, thus still allows accurate comparison between different measurements.

Figure 13: Studsvik 5310C neutron detector, mounted on the fusor at a distance of 48.7cm from the center.

Additionally, two identical detectors are placed on the ceiling and beneath the floor, outside the neutron shielding. Both are monitored simultaneously with the fusor-mounted detector. These detectors are intended to verify radiation safety towards adjacent rooms in the building, but can also double as consistency-check, allowing false measurements to be identified on the fusor-mounted detector. During high-voltage operation close to the maximum, it was noted that the neutron detectors are prone to noise, generating false pulses. An example of this is shown in Figure 14. Beyond the neutron shield a significantly lower neutron flux is expected, both due to the shielding and due to the added distance (inverse-square law). A significant illogical pulse recorded on the safety-detectors thus indicates a false noise-induced datapoint. When all three detectors simultaneously record a peak that deviates significantly from the background, the pulses on the fusor-mounted detector are discarded. While this operating regime is typically avoided for this reason, a limited amount of instability cannot be avoided during regular operations, as will be explained in section 3.4.

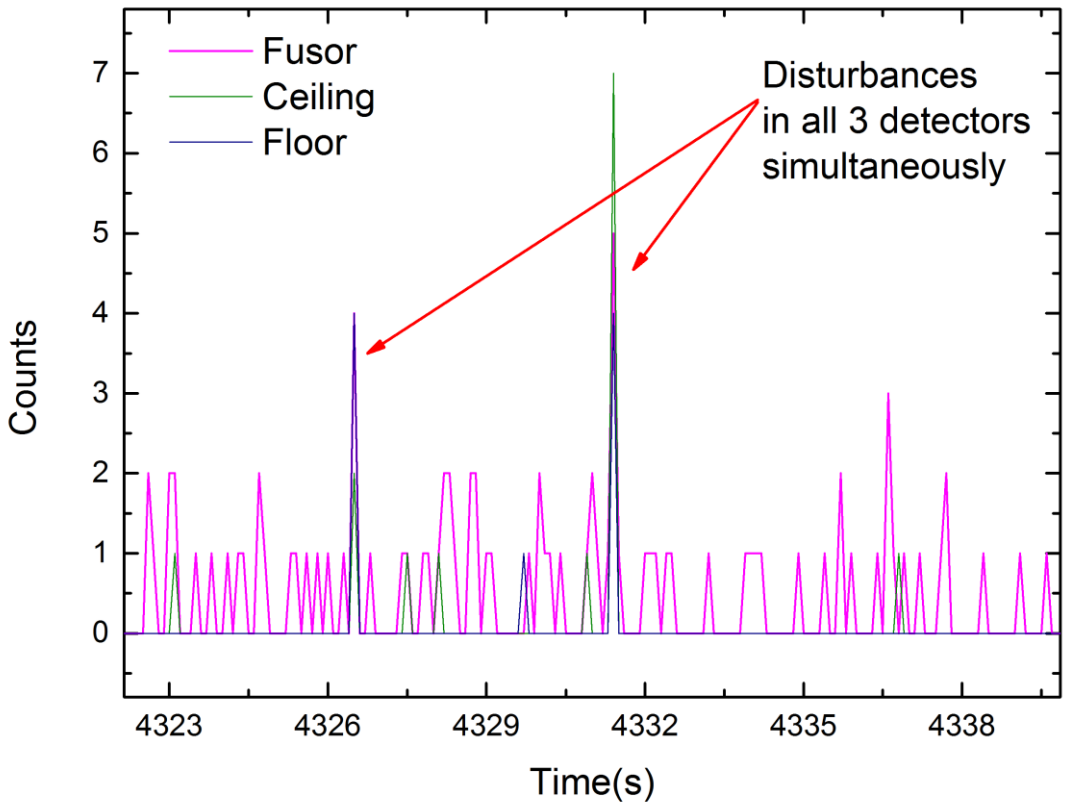

Figure 14: Raw measurement of counts in the neutron detectors. Pink: fusor-mounted neutron detector. Green: ceiling-mounted detector. Blue: detector mounted under the floor. When all three detectors show a simultaneous peak of more than 3 counts, the measurementis discarded.

3.4 Stability and reliability as a limiting factor for fusion operation

Apart from obvious limitations in terms of maximum current/voltage of the PSU and the minimum pressure in the vessel, the fusor exhibits more practical limits, mostly to do with reliability and stability. Stability during operation is paramount, since detecting the neutrons is, unsurprisingly, a difficult process while the neutron yield is relatively low. In most FUSOR operation modes, the Studsvik-detectors (see section 3.3) give <10 counts per second, meaning the statistical uncertainty is relatively large unless long and stable measurements can be made. The current, voltage and pressure should fluctuate as little as possible. Measurements of >60 seconds are the norm.

The two most limiting factors in terms of stability are the grid temperature and the HV-stability. Since the grid is not 100% transparent, the ion-grid interaction from fast ions bombarding the grid heat it up significantly, causing it to glow white-hot (see Figure 15). Above a certain temperature, the metal starts evaporating and outgassing impurities, which causes large variations in the fusor pressure and contaminates the pure D-plasma with foreign particles including metal vapor. When these instabilities occur, no accurate minute-long measurements can be made, hence a practical limit on the plasma current is reached. Additionally, the resulting metallic compounds in the plasma can coat the entire inside of the vessel (including electrical insulators and window ports) with a thin layer of metal, which should be avoided. This current limit is dynamic and depends on pressure (implicitly voltage), since at lower pressure the bombarding ions will have a higher E_{kin}, thus depositing more energy on the grid for the same current. The current-limit is visually determined in real-time by the operator through a live webcam.

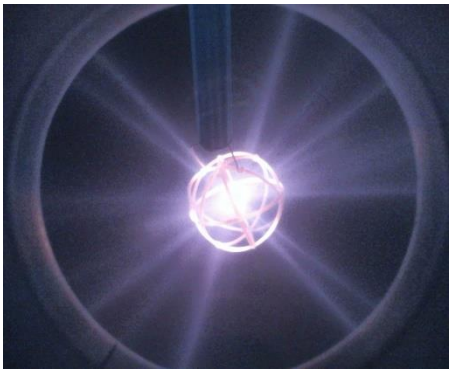

Figure 15: A white-hot glowing grid, heated by fast-ion bombardment of the grid wires during star-mode operation.

Secondly, the Studsvik-detectors appear to be sensitive to high-voltage instabilities (transients caused by sparking inside the fusor) which limits the useable discharge voltage range to a maximum of ~50 kV. Above this voltage, the grids starts shaking and the resulting noise on the neutron detectors renders the data useless. An attempt was made to reduce the noise by shielding the detectors with a grounded metal shroud. No reduction in noise during HV-instability was observed, so the exact origin remains unknown.

Finally, at very low pressures, regular plasma breakdown cannot be achieved without pushing the PSU well over 70kV, which is well above the HV-stability limit. As breakdown occurs, the discharge-voltage drops rapidly as soon as the plasma current introduces a voltage-drop over the resistor-stack (section 3.1.1), causing the plasma to fade. The result is a flickering unstable plasma combined with a shaking grid, which is not suitable for prolonged and accurate measurements.

3.5 Fusor operation and data analysis

This section will briefly describe how the fusor is operated and how the data is gathered, stored and analyzed.

3.5.1 Fusor control software

Since the fusor is a dynamic system, additional care needs to be taken to make sure the measurements are reproducible. To this end, a GUI interface had been designed that control some of the actuators on the fusor and gives real-time data the operators can use to reproduce their measurement accurately. A screenshot of this GUI is shown in Figure 16. The GUI runs in a Matlab environment.

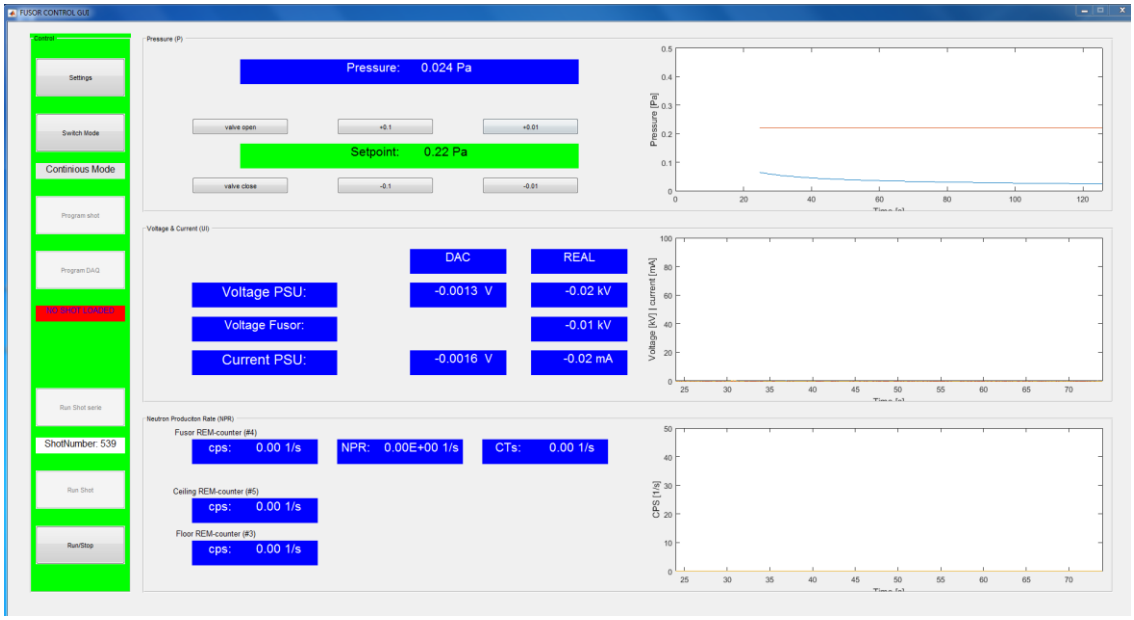

Figure 16: Screenshot of the Matlab based Fusor GUI. Voltage, current and corrected discharge voltage can be monitored in real time. Pressure and neutron counts are shown in real-time as well.

The GUI allows the pressure to be set, and transmits this to the RVC-300 controller (see section 3.1.1). The controller controls the EVR 116 stepper-motor valve to adjust the pressure until the setpoint is reached, and reports the actual pressure to the GUI with a frequency of 1 Hz. As such, an operator can be sure the desired pressure setpoint is reached before starting a measurement.

The Heinzinger HV power-supply outputs a proportional 0-5v for the operational ranges of both voltage and current. These outputs are connected to a National Instruments PXIe-6361 16 bits ADC which reports in real-time the output voltage and current to the GUI. Most importantly, the GUI uses the real-time current to adjust the reported voltage V_0 by the voltage-drop over the 210 kΩ ballast resistor to show the real-time discharge voltage V_d through formula (22)

This way V_0 can be adjusted in real-time by the operator to match V_d between shots of varying current. The output voltage and current are adjusted manually on the power supply itself.

Since the pressure is actively controlled and all relevant parameters are reported back to the operator in real time, the discharge can be adequately stabilized such that stable measurements of several minutes are possible.

3.5.2 Data analysis: voltage, current and neutron yield

As mentioned, the PSU voltage and current scaled on a 0-5V range are converted by a 16-bits ADC to be interpreted by the Matlab GUI. The neutron detectors are connected similarly, reporting individual counts to the software through the ADC. When a measurement is started, the voltage, current, pressure and number of neutron counts are recorded and saved with a frequency of 10 Hz. Pressure data is recorded with a frequency of 1 Hz. Afterwards, this data can be combined by their timestamps to yield a combined time-evolution of all these parameters in a single graph. As a result, for stable shots accurate measurements can be made by averaging over the entire shot.

For the neutron yield, the total number of counts during a single measurement is divided by the duration of the measurement to yield the number of counts per second, or *cps*. Since the counting of neutrons is a Poisson-distributed process in nature, the error is easily calculated in terms of 68% intervals by taking the square root of the total number of counts.

4 Results

4.1 Fast ion population

One of the most important parameters in nuclear fusion is the energy of the plasma particles, since the fusion cross-section strongly depends on it – generally higher is better. As explained before, many fusor ions will not benefit from the full electric potential and are essentially 'wasted' when their energy is too low to fuse. Using an ion source at the edge of the plasma, an attempt is made to increase the fraction of fast particles. In the following sections, spectroscopy will be used to monitor the effects of the ion source on the ion energy distribution as described in section 3.2.2. These results will be used to verify whether an increase in the fast ion population can be directly correlated to neutron yield increases.

4.1.1 Hydrogen and deuterium discharges without ion source

As mentioned, the Doppler shift is of main interest in analyzing H and D spectra, since it acts as the main indicator for the presence (and amount) of fast radiating species inside the fusor. Figure 17 shows a typical spectrum of a hydrogen star-mode fusor plasma (see section 2.2.2) operating at 0.13 Pa with a fusor potential of (45.2 ± 0.6) kV.

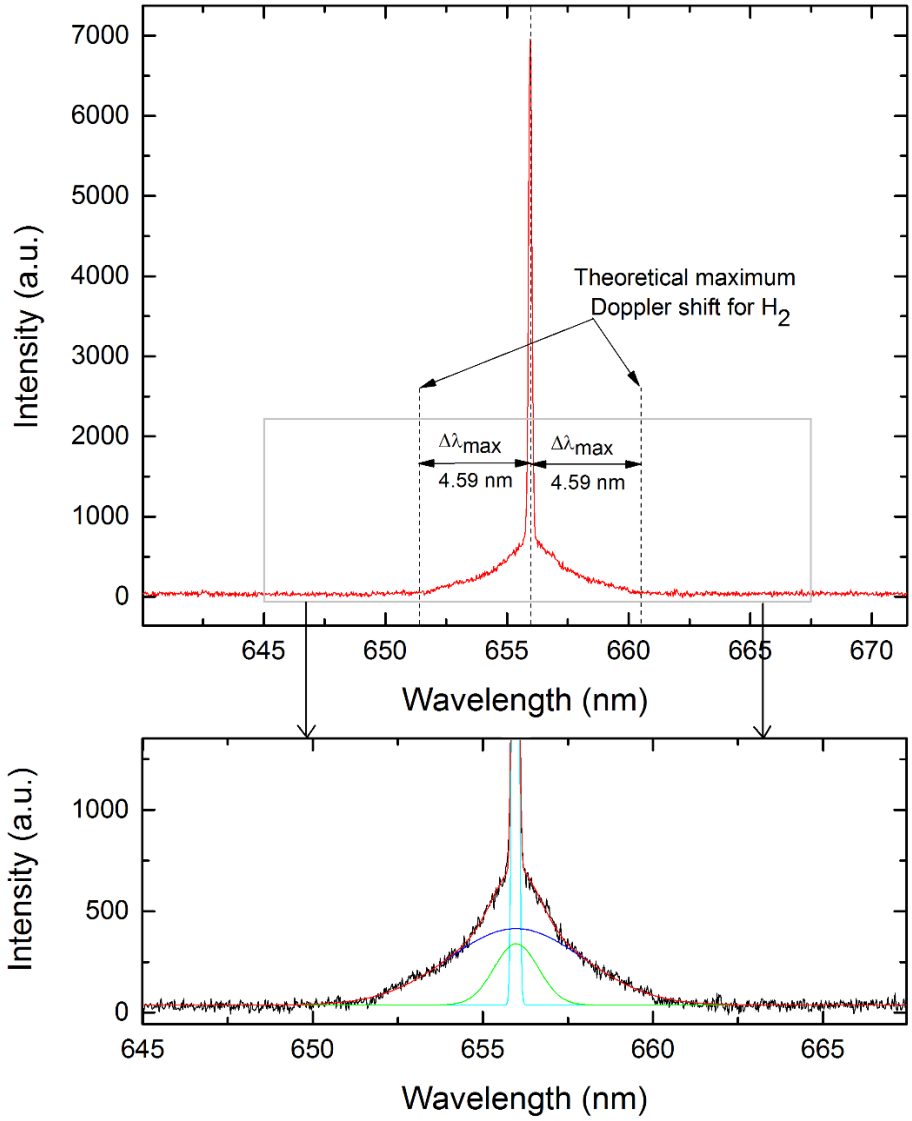

Figure 17: Typical spectrum of a star-mode hydrogen plasma at 0.13 Pa with a fusor potential of (45.2 ± 0.6) kV. The dotted lines show the maximum theoretical Doppler broadening ($\Delta\lambda_{max}$ = 4.59 nm) that should be observed for H_2^+ particles accelerated by the full fusor potential of (45.2 ± 0.6) kV and undergoing dissociation to H^* and H^+. The bottom panel shows a triple Gaussian fit.

Two distinct features can be distinguished in this particular spectrum; a central peak at the H-α 656 nm line showing the contribution of the mostly stationary plasma in the center of the grid, and a wide Doppler-broadened profile that corresponds to the contribution of the dynamic fast oscillating particles. As mentioned in section 3.2.2, since the broad distribution is the result of several independent factors with yet uncharacterized behavior, fitting that profile with 5 or more independent distribution functions would be arbitrary and yield no new information without a priori knowledge on the plasma composition. The central peak, however, can be analyzed since the stationary plasma dominates the contribution to this line.

To accurately fit the central peak and obtain its FWHM, a triple-Gaussian fit was performed such that the broad feature was taken into account by the combination of two broad Gaussians, and the remaining narrow Gaussian accurately describes the broadening of the peak. The fit is shown on the right panel of Figure 17. The total $\Delta\lambda_{FWHM}$ of the central narrow peak is (0.160 ± 0.005) nm. Since this is close to the instrumental broadening of (0.12 ± 0.01) nm (see section 3.2.1), the thermal and instrumental broadening need to be deconvoluted from this peak by formula (21) in section 2.4.5. Assuming only thermal broadening, the resulting $\Delta\lambda_{FWHM}^{Doppler}$ = (0.11± 0.02) nm, which for a hydrogen plasma corresponds to an average ion temperature of (4.4 ± 1.6) eV. The error analysis can be found in Appendix A.

It is expected that the broad feature accompanying the central narrow peak is the result of several different species with a yet unknown particle energy distribution. These species eventually break down into H^*, which contributes to the Doppler-shifted feature. Therefore it cannot be fitted by a single Gaussian, and a physically correct convoluted fit would require a priori knowledge on the amount of visible species in the plasma and the scaling of the physical factors that influence the shape of the broadening profile. In section 3.2.2 these physical factors were discussed. The double-Gaussian fit of the broad feature next to the central peak thus cannot be expected to paint a complete physical picture, but will be discussed further in section 5.1.1.

More qualitatively, the total width and intensity near the edges gives a hint on the possible nature of the species contributing to it. The decay in intensity for higher $\Delta\lambda$ indicates only a small fraction of fast particles emit while at maximum kinetic energy, as expected (see section 2.3.1).

Note that only atomic hydrogen can contribute to the Balmer-α emission line; any Doppler-shifted Balmer-α emission must originate from an H^* emitting at some velocity. Ignoring (for now) the exact mechanisms, if it is assumed that a molecular ion containing H breaks up into at least one H^*, which necessarily has the same linear velocity as the parent species, the Doppler-shifted emission of this particular H^* can be used as a measure for the velocity of the parent species. This way, species that do not radiate on the Balmer-α line can still show up as a Doppler-shifted feature in the Balmer-α Doppler broadening profile.

Since in a hydrogen plasma H_2^+ is expected, indicative dotted lines were drawn that correspond to the Doppler-shift a H_2^+ ion would give (through emission of the H^* after dissociation) if it obtained the maximum possible kinetic energy $E_{max} = eV_d$ from the 45.2 kV discharge potential ($\Delta\lambda$ calculated by formula (17) in section 2.4.3.2). The broadening pattern fits between these lines, indicating the spectrum most notably shows contribution of the H_2^+ plasma population at an unknown distribution of energies. This will be expanded upon in section 4.1.2. Note that fast H^* at $E_{max} = eV_d$ is not directly observed in this spectrum, since that would require a visible contribution up to $\Delta\lambda_{max}$ of ~6.5nm due to the difference in mass. In experiments using an ion source, fast H^* at the maximum possible velocity *is* observed, as will be shown in section 4.1.2.

The goal of this thesis is to determine whether the fast ion fraction can be increased and if this increases the neutron yield. Intuitively, not being able to characterize the baseline energy distribution from the spectra (for the reasons mentioned above) would seem problematic. However, while an exact quantitative analysis is difficult, a comparative study between similar situations is not; since all geometrical factors remain the same when adding an ion-source, the direct effects of the ion source on the plasma can be observed and analyzed without a complete quantitative description of the spectrum and plasma species. As will be shown in the next section, using an ion source at the plasma edge significantly alters the spectrum such that quantifiable features appear.

4.1.2 Discharge with ion source – using the ion source as a plasma diagnostic

Figure 18 shows the spectra of an ion-source assisted H-plasma (blue) and a D-plasma (red) overlapped, operated at low pressure (0.13 Pa and 0.17 Pa respectively). Firstly it is noted that the central wavelengths of the Ballmer-α peaks were recorded at λ = (656.00 ± 0.01) nm for H and λ = (655.83 ± 0.01) nm for D by fitting a Gaussian through the central peak. While these differ by 0.29 nm from the literature value of

656.29 nm and 656.11 nm respectively, the difference of 0.18 nm between D and H correctly manifested in these measurements. As the analysis is performed in terms of $\Delta\lambda$, this systematic (calibration) error in λ is automatically eliminated and does not affect the results.

Similarly to section 4.1.1, FWHM was recorded for both sharp D and H peaks and determined to be (0.16 ± 0.01) nm for H and (0.14 ± 0.01) for D. After deconvolution with the instrumental broadening, the resulting central plasma ion temperatures are determined to be (4.4 ± 2.2) eV for H_2 and (8.8 ± 6.0) eV for D_2. This result is further discussed in section 5.1.2.

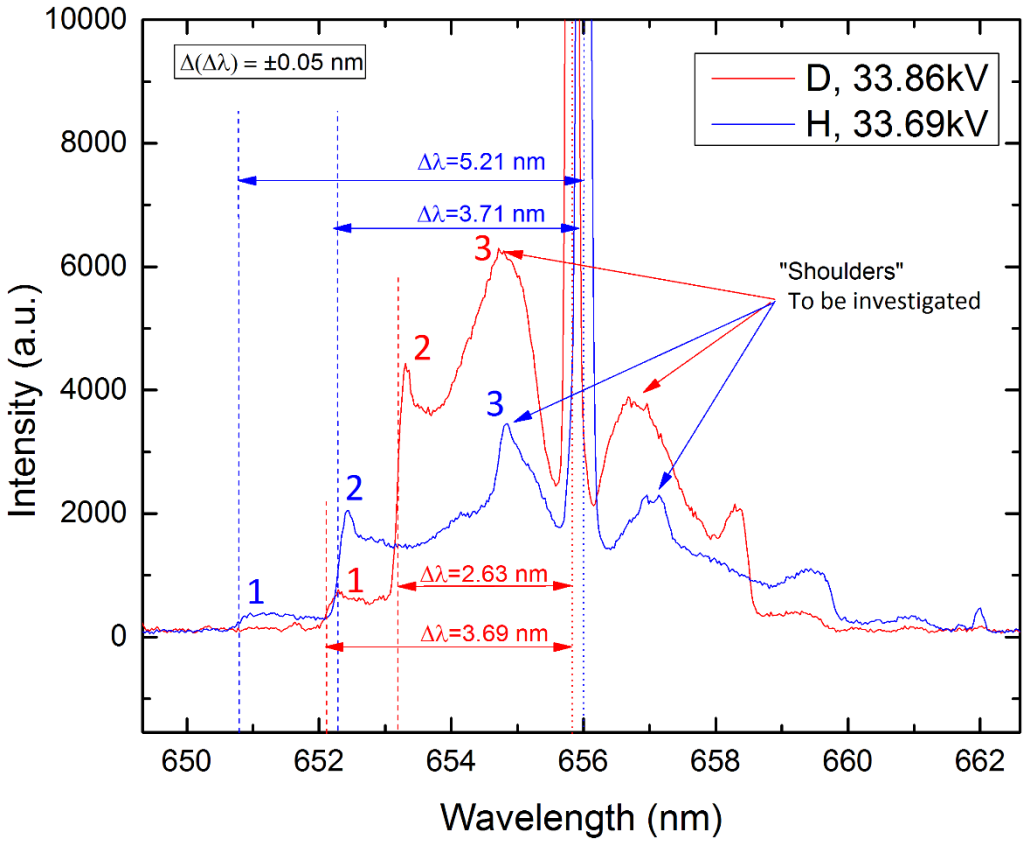

Figure 18: Spectrum showing the Ballmer-alpha lines of a D-plasma (red) and H-plasma (blue) under similar conditions, with the ion source injecting the ions at the edge of the vessel. Features of interest are numbered and will be referred to as "feature 1", "feature 2" and "feature 3".

In this measurement, the discharge voltage is kept sufficiently low (~33.7 kV) in order to avoid breakdown to full star-mode, resulting in a single beam through the center. In such case, most – if not all - of the ions will originate directly from the source and are accelerated towards the center by the full fusor potential. It is expected that this results in a reasonably mono-energetic energy distribution of the injected species when this population reaches the center. In a spectrum, this should manifest as a (peaked) increase in emission at high values of $\Delta\lambda$ compared to a regular star-mode plasma. Figure 18 shows such behavior, contrasting the 'smooth' decreasing Doppler-shift distribution of Figure 17. Additionally, pedestal-like features are observed that end in a sharp drop-off (ridge) above a specific wavelength. These ridges are annotated with the dotted vertical lines and numbered 1 and 2, and can be used to identify different plasma species. Note that the leftmost ridge (feature 1) of the hydrogen spectrum ($\Delta\lambda$ = 5.21) is not accompanied by a definite peak, while the ridge of feature 2 ($\Delta\lambda$ = *3.71)* is. The two 'shoulders' (feature 3) visible at ~655 and ~657 nm should also be noted, and will be discussed later on.

Without needing to know the exact shape of the energy distribution, the steepness of the ridge in both features 1 and 2 suggest the presence of a hard limit in $\Delta\lambda$ for a specific population of atomic H and D. The accompanying peaks for the features numbered 2 at $\Delta\lambda$ = *2.63* nm (red spectrum) and $\Delta\lambda$ = 3.71 nm (blue spectrum) strengthen the notion that these Doppler-shifted features indicate a near-mono-energetic population. For the features numbered 1 this peaked behavior is missing, indicating a population with a more evenly distributed energy distribution. Note that feature 1 shows significantly higher emission compared to Figure 17, where no emission could be observed at all at the same $\Delta\lambda$.

When analyzing the Doppler-shift of feature 2, it is noted that no potential difference inside the fusor exists that corresponds to atomic H and D being accelerated specifically to these values of $\Delta\lambda$. As explained in the previous section, such definite and deviant populations can be interpreted as originating from a larger (heavier) parent species that contained atomic H or D and dissociated into at least one excited atomic specie (H^* and D^*) with identical linear velocity.

By using the uniqueness of the weight of possible parent species, the species responsible for the ridges in the spectrum can now be identified. By noting that singly charged ions are accelerated over the full potential, all of these different ions will gain identical amounts of $E_{kin,max} = e|V_d|$ from the electric field while they differ in mass. Therefore, from $E_{kin,max} = {}^1/_2\, m{v_{max}}^2$, species with a unique mass at the same E_{kin} will show uniqueness in measured values of v_{max} and thus $\Delta\lambda_{max}$. Therefore the locations of these ridges are used to identify the species responsible for them. The remaining characteristics of the broadening profile are discussed in section 5.1.2, where an attempt is made to fit the peaks to create a good envelope fit. For the remainder of this section, however, it is not necessary to deconvolute the spectrum in its totality, as the main argument is based on characterizing the maximum energy of a mono-energetically injected population of ions without prior knowledge on the exact shape of the energy distribution.

In Table 1, E_{kin} is calculated (in keV) from the measured values of $\Delta\lambda$ for different hypothetical masses (formula (17), section 2.4.3.2). The resulting energies are then compared to the fusor potential, which should show a close to 1:1 correlation in magnitude for singly charged species. Combined with knowledge on the source gas (D_2 or H_2), the species responsible for the individual ridges in the spectrum can be identified.

Table 1: Particle energy as calculated from the Doppler shift for different hypothetical masses. Highlighted cells correspond best to the fusor potential. Combined with knowledge of the source gas (red cells = D_2 gas, green cells = H_2 gas), possible species corresponding to this mass are listed.

Δλ (nm)	*Corresponding E_{specie} if m = 1u*	*Corresponding E_{specie} if m = 2u*	*Corresponding E_{specie} if m = 4u*	*V_{fusor} (kV)*	*Radiating species*	*Fast parent species*
2.63	7.46 keV	14.9 keV	***29.8 keV***	33.86 kV	**D^***	**D_2^+**
3.69	14.7 keV	***29.3 keV***	58.6 keV	33.86 kV	**D^***	**D^+**
3.71	14.8 keV	***29.6 keV***	59.3 keV	33.69 kV	**H^***	**H_2^+**
5.21	***29.2 keV***	58.3 keV	117 keV	33.69 kV	**H***	**H^+**

Using the information listed in Table 1, feature 2 in the D-spectrum of Figure 18 can be identified as indicating D_2^+ for $\Delta\lambda = 2.63$ *nm* since the resulting velocity is consistent with a particle mass of approximately 4u with E_{kin} = 29.8 keV (<33.86kV). Similarly, in the H-spectrum the $\Delta\lambda = 3.71$ *nm* corresponds to H_2^+. Both features 2 at $\Delta\lambda = 3.69$ *nm* and $\Delta\lambda = 5.21$ *nm* correspond to D^+ and H^+-ions respectively. The mechanism through which the radiating species are created from the 'fast parent species' as listed in Table 1 is discussed further below.

First, the hypothesis that these ridges indeed correspond to an $E_{kin,max}$ needs to be verified. To this end, a voltage-scan was performed where the ridges in the spectrum are expected to shift further outwards as the discharge voltage increases. Results of such scan are shown in Figure 19 for a D-plasma.

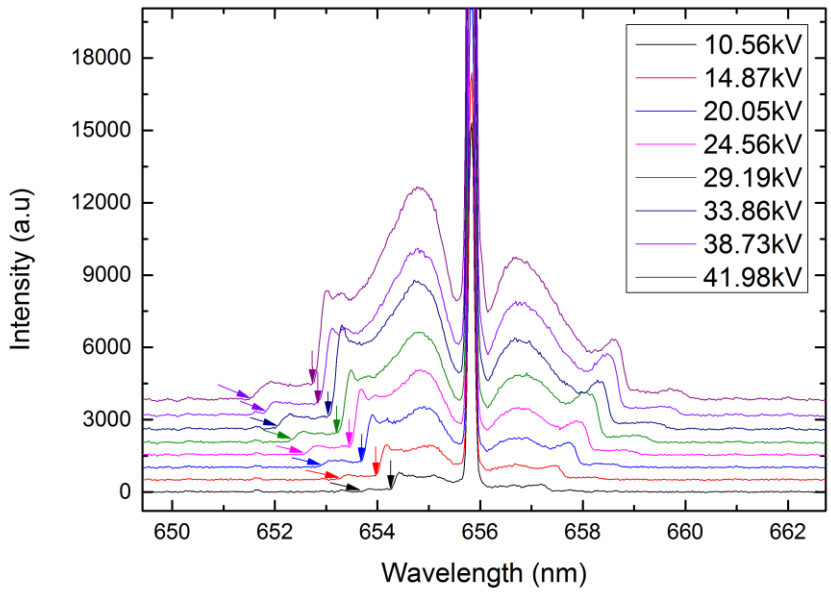

Figure 19: Deuterium spectra resulting from a voltage scan at 0.17 Pa. Spectra are offset by 500 counts each for better visibility. The ridges visibly shift in proportion to the discharge voltage. Datapoints are taken as 'maximum particle velocity' from all locations indicated with the arrows.

Figure 19 shows 8 superimposed spectra of a deuterium plasma at 8 different fusor potentials. Each spectrum has been offset by a value of 500 counts for better visibility. While the shapes of the central peaks do not change significantly (except in intensity), the ridged features indeed shift with increasing fusor potential as expected. Data-points are collected at the base of each ridge. This is justified in noting that no species can physically reach energies above eV_d. Thus for each specie the base of the ridge should be close to – but not higher than – the maximum kinetic energy eV_d. This yields a larger error than fitting the peak, however analysis of the peak of the resulting energy distribution would not necessarily correspond to the maximum attainable energy, depending on the exact energy distribution of each specie. While a mono-energetic component in the energy distribution is expected due to the ion source, contributions of slower particles and contributions of the 5 factors listed in section 3.2.2 will shift the peak of the total observed distribution away from the maximum energy. As such, analysis of the slightly less accurate (but more precise to the parameter of interest) base peak is preferred.

To characterize the correlation between Doppler-shift and discharge voltage, a plot of this discharge voltage vs. the particle energies as calculated from $\Delta\lambda$ is shown in Figure 20. The black datapoints (big ridges, corresponding to D_2^+) and the red datapoints (small ridges, corresponding to D^+), both exhibit a linear correlation with the discharge voltage as expected, and correspond well to the maximum kinetic energy that can be gained from the field (denoted by the green line).

It is now possible to address the possible mechanics that lead to the identified species showing up in the Balmer-α Doppler-broadening profile. As mentioned, only atomic hydrogen has the ability to emit Ballmer-α photons. Three options (where applicable listed with relevant cross-sections) are proposed as possible mechanism for the creation of fast H^* (and similarly D^*) with identical velocity to the fast source particle:

1) Charge-exchange / recombination for fast H^+ source particle:

   $H + \text{fast } H^+ \rightarrow H^+ + \text{fast } H^*$ ($\sigma(50\text{keV}) \sim 10^{-16}$ cm^2) [24]

   $e + H^+ \rightarrow H^*$

2) Electron-impact dissociation for H_2^+ molecular ions

   $e + H_2^+ \rightarrow e + H^+ + H^*$ ($\sigma \sim 4 * 10^{-16}$ cm^2 for $E_e \sim 30$ eV)

   ($\sigma \sim 4 * 10^{-17}$ cm^2 for $E_e \sim 1$ keV) [26]

3) Energy transfer through elastic collision with an excited background molecule

$H_2 + H \rightarrow$ Momentum Transfer $\quad (\sigma < 10^{-20}\ cm^2$ for $E_i > 10keV)$ [27]

Options 1) and 2) should be the dominant mechanisms for producing H^* with velocities identical to the source particle. Based on the cross-section for option 3), momentum transfer can be assumed a benign process compared to the others as they differ by 4 orders of magnitude for their relevant corresponding energies. Momentum-transfer can be further disqualified for the features numbered '2' in Figure 18, since a H_2^+ source particle colliding elastically with H^* will yield a H^* of significantly higher velocity due to the difference in mass.

The cross-section for 1) scales with the density of the background gas, and since the background gas pressure is constant throughout the vessel, these reactions can occur anywhere in the vessel. The cross-section for 2) scales strongly with the electron energy. Since slow electrons can only be found close to and in the center of the grid, this reaction process should predominantly occur there. Consequently, as ions only travel at maximum velocity in the center of the grid, a mono-energetic population of H_2^+ should create a mono-energetic population of H^*, which should show up in the spectrum as a narrow Doppler-shifted peak. This is exactly what is observed in the corresponding spectral feature (numbered '2'), which shows a significant fraction of the observed fast neutrals are at or close to $E_{kin,max}$.

Feature number '1' does not show such peaked behavior, which can be explained by noting that – if charge exchange is the dominant mechanism – charge exchange can occur anywhere in the vessel. This means photon emission occurs in-between both concentric electrodes, where the particle is at a velocity below v_{max}. Thus while the population is mono-energetic in the center of the of the grid, the distribution of the resulting emission in the Doppler-broadened profile need not be.

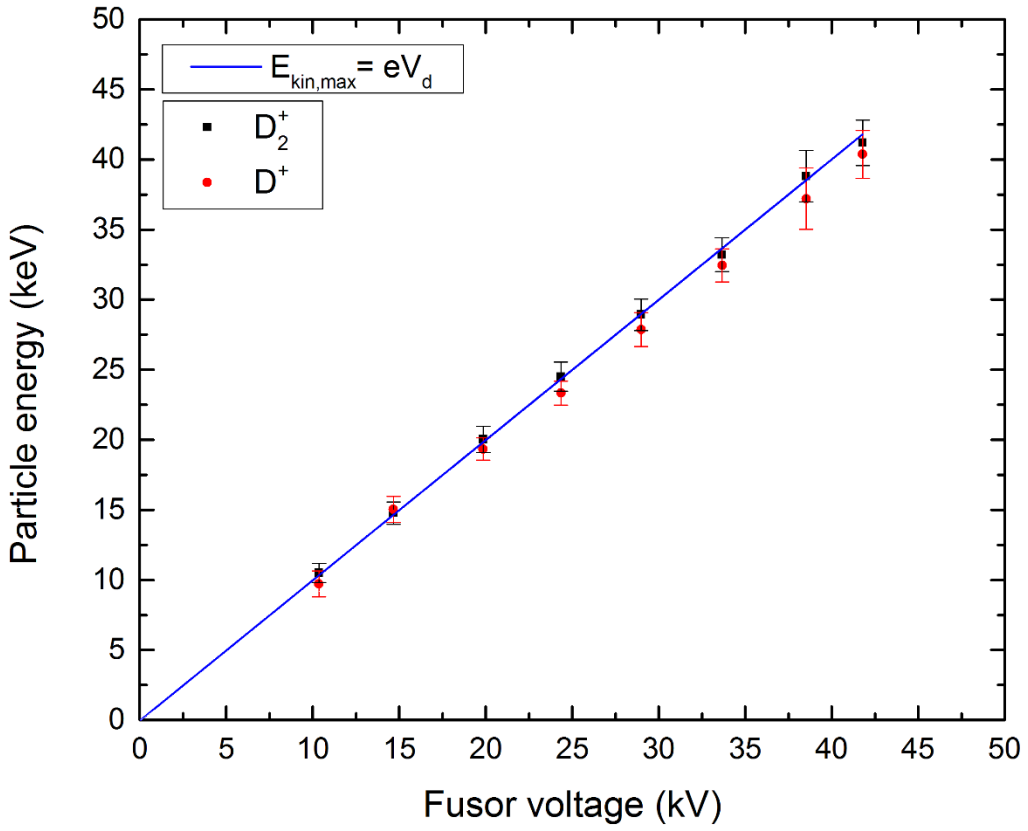

Figure 20: Plot of particle energies for D_2^+ (big ridge, black datapoints) and D^+ (small ridge, red datapoints) compared with the discharge voltage. The blue line indicates the expected maximum particle energy for D_2^+ and D^+ originating from the ion source.

Finally, the 'shoulders' as indicated in both Figure 18 and Figure 19 make a significant contribution to the Doppler-shifted profile, especially so at higher discharge voltages. However, contrasting the contributions of D_2^+ and D^+, these features lack a distinct ridge thus cannot be easily interpreted in terms of $E_{kin,max}$. Therefore instead of analyzing a ridge, a 4th order polynomial was fitted through the

'shoulders' to accurately determine $\Delta\lambda$ at the maximum. A plot of $(\Delta\lambda)^2$ as a function of the discharge potential shows how the shift-behavior of these features scales, and is shown in Figure 21. This plot should indicate if the average energy (which is proportional to $(\Delta\lambda)^2$) of the species responsible for these peaks scale linearly with the discharge potential.

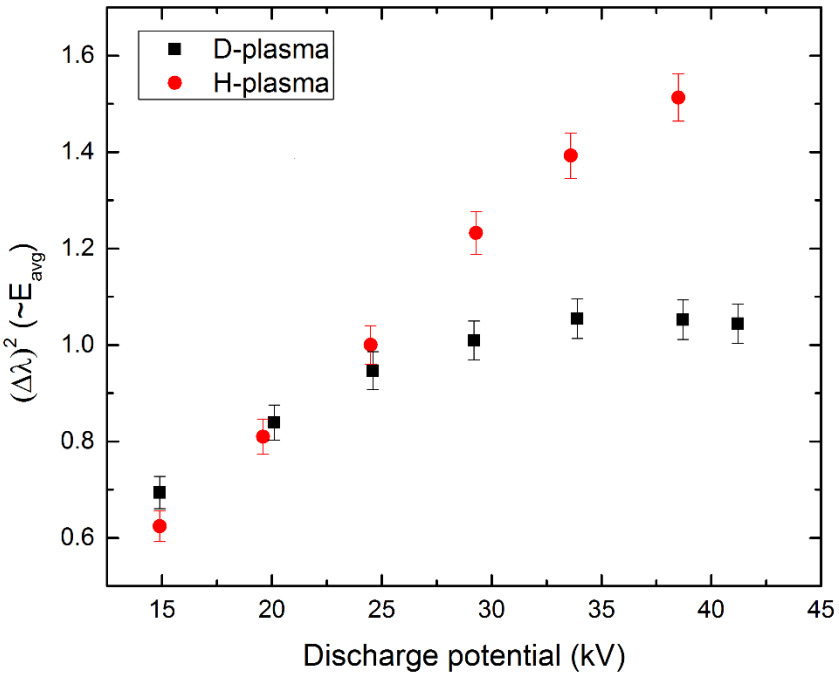

Figure 21: Plot of $(\Delta\lambda)^2$ as a function of the discharge potential. For the hydrogen voltage-scan, a linear correlation can be observed, while in the deuterium plasma a plateau is observed.

Since Figure 21 shows a linear increase in hydrogen, it can be concluded that the average energy of the species responsible to these peaks scales linearly with the discharge potential, just like H_2^+ and H^+. In the deuterium plasma, the shift plateaus and the same conclusion cannot be drawn. Since no definite ridge is observed, and no hard limit in Doppler-shift for these species can be assigned, no estimated weight can be attributed to these species, and thus remain unidentified. Fortunately, these features are of lesser importance to the research questions in this work, since D_2^+ and D^+ have already been successfully identified.

4.1.3 Fusion yield scaling – without ion source

Before the effects of the ion source on neutron yield can be discussed, an analysis must be made of the neutron yield without it. Such analysis is not trivial, as the two parameters most correlated to the neutron yield, namely voltage and current, are difficult to decouple. Pressure, discharge voltage and fusor current all affect the neutron yield and are all interdependent on one another. As discussed in section 3.5.1, special care is taken to accurately determine the discharge voltage due to the voltage-drop over the ballast resistor at high currents.

General scaling was observed to be as follows:

1) Discharge voltage: increasing voltage increases neutron yield, since the fusion cross-section depends strongly on the kinetic energy of the ions (see Figure 3 in section 2.1.2). Since the maximum voltage of the fusor is only ~60 kV (below the ideal D-D energy), generally the voltage is kept as high as possible.

2) Discharge current: increasing the current generally shows a corresponding increase in neutron yield for the same voltage. An increase in plasma current indicates an increased amount of ions hitting the grid, which – for the same pressure – indicates an increase in the ion number density. This should give an increase in neutron yield.

3) Gas pressure: increasing the pressure affects both current and voltage; the current is increased while the maximum voltage is limited. When operating in star-mode, a higher pressure yields an easier to ignite (stronger) plasma, which is observed through an increased plasma current

(increased ion density). Neutron yield will generally increase accordingly. However, upon further increase of the pressure, the current limit of the power supply is reached, limiting the maximum voltage. Similarly, if the current needs to remain constant, an increase in pressure will decrease the discharge voltage, decreasing neutron yield. At pressures above 0.5 Pa, no more fusion is observed due to the low corresponding voltage.

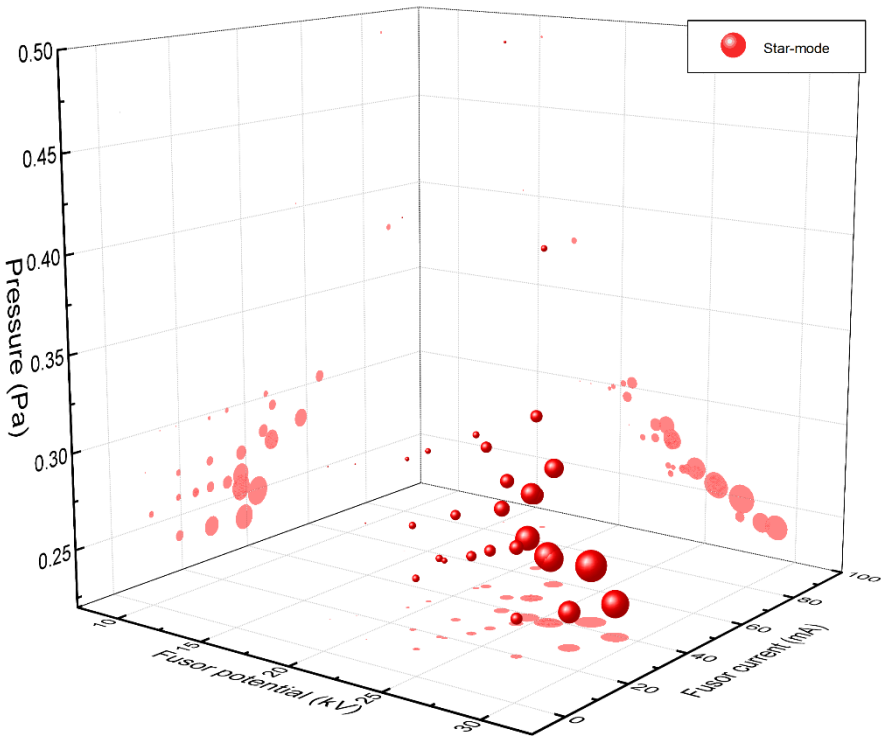

Figure 22: 3D scatterplot of the neutron yield for varying voltage, current and pressure. The diameter of the balls scale proportionally to the neutron yield. A table containing all data including uncertainties (not plotted here) can be found in Appendix A.

Figure 22 shows the operational regime of the fusor for pressures as low as 0.24 Pa using the titanium grid (see section 3.1.2). This 3D-plot shows the result and dependency of the 3 aforementioned scaling-parameters for a regular star-mode plasma. The diameter of the balls scale proportionally to the neutron yield, bigger indicating more neutrons per second. The datapoints shown span the entire operational regime that is stably attainable before hitting the stability- and reliability-limits as described in section 3.4; higher voltage/current at set pressures could not be sustained stably without risking damage to the fusor, while at pressures below 0.24 Pa no stable discharge breakdown could be maintained. This plot illustrates the difficulty in benchmarking the fusor while independently controlling voltage, current, and pressure, since these are always linked.

Evidently, the neutron yield increases as pressure drops, since the lower pressure allows a higher stable operating voltage to be reached before hitting the current-limit. The neutron yield thus scales strongest with the voltage, as expected from the strong increase in fusion cross-section, outpacing the positive linear scaling with background gas pressure described by formula (4). In this mode of operation, the maximum fusion yield, corresponding to the measurement at 28.9 kV, 39.2 mA, and 0.24 Pa was determined to be $(4.35 \pm 0.39)*10^5$ neutrons/second (68% error interval, see Appendix A).

Figure 22 suggests that operation at lower pressures could see higher neutron yields. The ion source can be used to 'unlock' this operational regime, the results of which are discussed next.

4.1.4 Fusion yield behavior - with ion source

As mentioned in section 3.4, the main problem with operating at low pressure is that the plasma ignition and sustain becomes unstable. The main issue is the plasma occasionally fading. As the current drops to 0, the discharge-voltage shoots up since the voltage drop across the ballast resistor disappears, and re-

ignites the plasma violently. Usually this results in noise on the neutron-counters. Multiple instabilities in rapid succession could be dangerous, as the grid can start shaking uncontrollably.

Turning on the ion source mostly mitigates these instabilities, since the direct injection of ions keeps the discharge from fading. The ion injection increases the plasma current while the voltage across the fusor drops slightly, resulting in a more stable operation. Moreover, extremely low pressures – where regular discharge breakdown does not occur – can now be reached. The resulting neutron yield in this 'unlocked' regime is shown in Figure 23 in the same style as Figure 22.

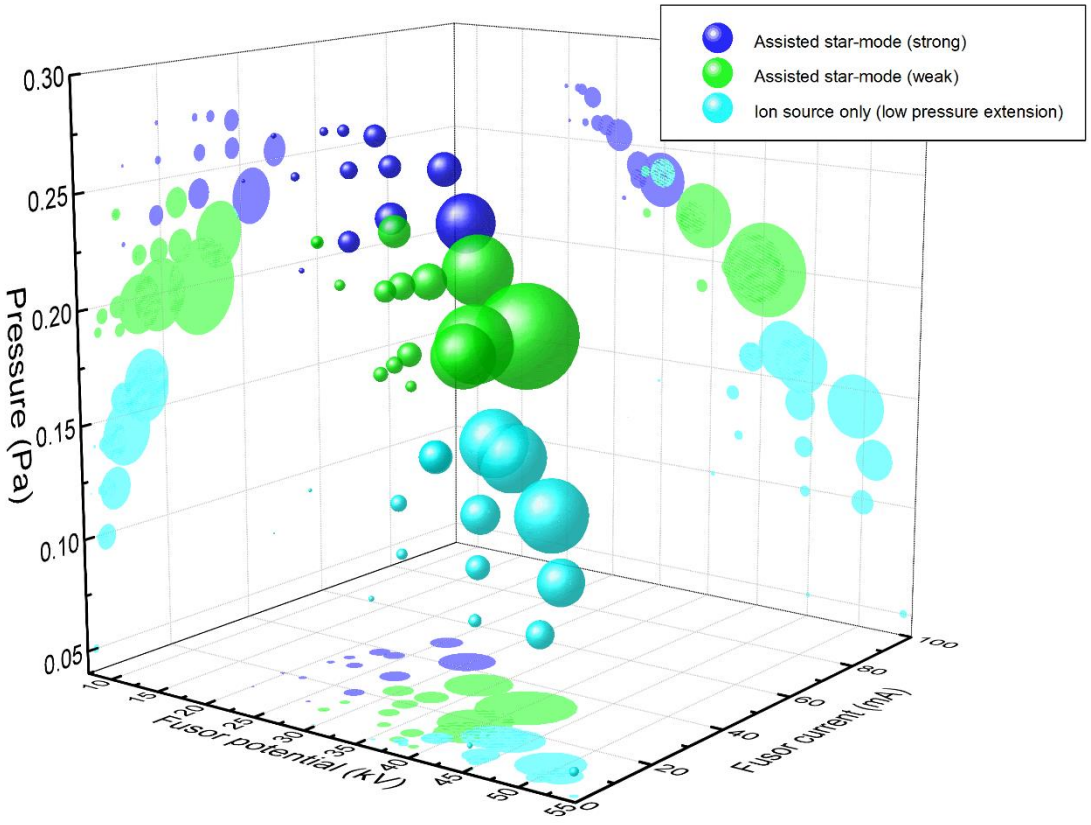

Figure 23: 3D scatterplot of the neutron yield for varying voltage, current and pressure while using an ion source to stabilize the discharge. The varying colors indicate different ion-source settings. The diameter of the balls scale proportionally to the neutron yield. Precise data is listed in Table 2 in Appendix A.

The measurements have been subdivided in 3 sets, color-coded blue, green, and light-blue. The green set is a general extension to Figure 22, where the ion source is used at low power only to stabilize the plasma, indicated by "weakly assisted star-mode". The discharge is still in star-mode and thus exhibits general breakdown, where the current can be increased up to the limit set by the grid temperature. Compared to Figure 22, higher voltages are reached and at maximum current an increased neutron yield is observed. The maximum yield at 40.1 kV, 29.8 mA, and 0.20 Pa was measured to be $(1.43 \pm 0.14)*10^6$ neutrons/second.

The light-blue series were measured at such low pressure that general star-mode breakdown no longer occurs at voltages <55 kV (above which HV noise disturbs the neutron detectors, see section 3.4). The ion source (at high power) is now fully responsible for the plasma, which manifests as a single beam through the center. At the lowest pressures, the plasma current is no longer limited by the grid-temperature, but by the amount of ions the ion source produces. To maximize the neutron yield for this specific experimental setup, a balance has to be found between the pressure and the plasma current, as increasing pressure now does increase the current at a relatively constant voltage due to a limited capacity of the ion source. The resulting maximum neutron yield at 49.1 kV, 10.7 mA, and 0.14 Pa was measured to be $(8.79 \pm 0.34)*10^5$ neutrons/second. It is expected that significantly higher neutron yields can be achieved if higher currents can be reached at the lowest pressures, since in this regime the discharge is

not limited by constraints on the grid temperature (see section 3.4). A proposition for a design-improvement to achieve this will be discussed in the outlook (section 6.1).

Finally, the blue data-points show a comparative set of measurements exploring the same regime as Figure 22, now combined with the ion source at high power. Any direct effects of the added ion source can then be compared to a stable star-mode plasma configuration. These datapoints have been overlapped with each other, resulting in the plot shown in Figure 24.

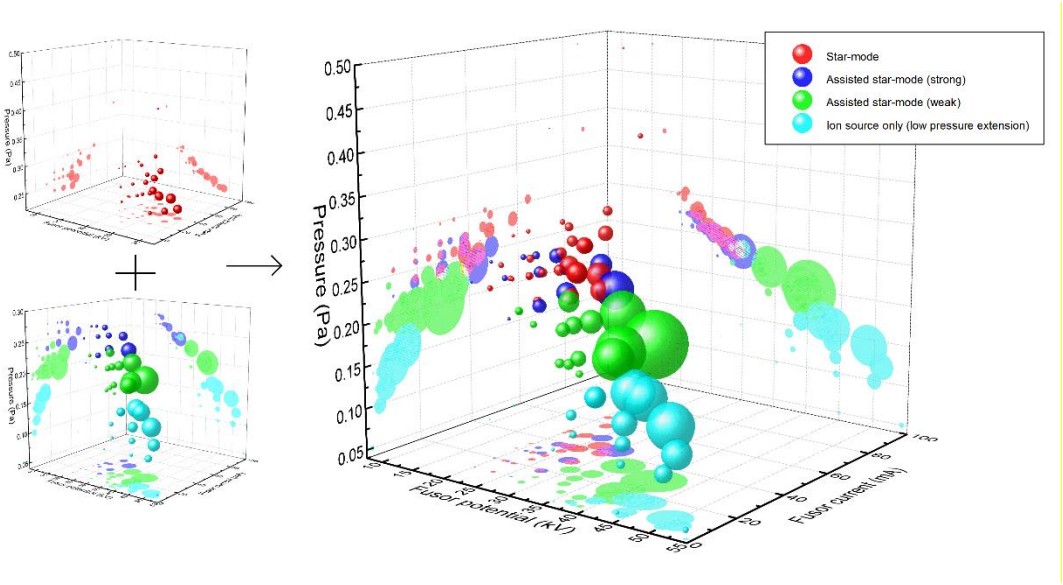

Figure 24: Combined plot of Figure 22 and Figure 23. No significant differences in terms of neutron yield can be observed in the overlapping part.

As shown in this plot, adding the ion source does not significantly increase the neutron yield when comparing the red and blue data-points. One outlier – the biggest dark-blue data-point – was observed as the plasma happened to be more stable at a slightly higher voltage and current compared to the best red data-point. All other data-points show roughly the same neutron yield, indicating the ion source has little to no effect in this region. Possible explanations for the lack of effect of the ion source are discussed in section 5.

4.2 Deuterium loaded target

As it is theorized that the fusion yield scales as $n_i n_g \langle \sigma v \rangle$ [5], simply increasing n_g or n_i seems straightforward. However, as shown in section 4.1.3 and 4.1.4, increasing n_i is not always possible while increasing n_g through increasing the pressure proved to be detrimental to neutron yield due to a significant corresponding decrease in $\langle \sigma v \rangle$. One alternative to increasing n_g without increasing the gas pressure, is to embed large amounts of D in the top-layer of a metal target. Titanium was chosen as a target material. Since Ti can hold several orders of magnitude more D-atoms compared to the absolute amount of background gas within the grid (see section 2.3.2), this option was explored in two ways:

1) Altering the grid material to titanium to repurpose inherent grid-losses into fusion-reactions
2) Inserting a titanium target to be loaded with D in the center of the grid

Target materials were benchmarked in pristine condition, followed by typically ~1 hour of 'loading' as described in section 3.1.2. After loading, the benchmark is repeated and the results compared.

4.2.1 Exploratory test results on Ti target inside W grid

Deuterium loading was performed inside the fusor with a high-pressure plasma at ~5-10 kV for ~30 minutes, leading to an expected ion fluence of ~10^{17} D/cm^2 (see Appendix B). After loading, the target was bombarded by a high-energy star-mode discharge. As mentioned in section 2.3.2, a target with a total surface area of 14 cm^2 (double-sided) is expected to contain 10-100 times more D than the background gas contained within the grid. As such, effects were expected to be significant enough to see immediate results. Initial results indicated an increase of ~50% in fusion yield, however these tests were

performed in the early stages of the project, when operation characteristics of the fusor were yet to be accurately determined. The data of the initial tests was deemed unsuited for in-depth analysis as the discharge voltage and current were not directly comparable between both measurements.

It was observed that a target suspended in the center of the grid blocks part of the plasma, and introduces difficulties in maintaining a discharge. To eliminate a solid target without losing benefits of embedded-fusion, a new grid was constructed from titanium. Effectively this utilizes the unavoidable ion-grid interactions for additional fusion, without disturbing the central plasma.

4.2.2 Exploratory tests on a small Ti grid

The titanium grid was constructed from Ø(2 mm) Ti-wire, resulting in the Ø(6 cm) grid shown in Figure 9. Relatively thick grid wires (compared to the 0.44 mm wire gauge used in the W grid) were used to stimulate ion-grid interactions, as these were expected to significantly increase neutron yield. Initial tests with a pristine non D-loaded grid showed a significantly reduced neutron yield at similar voltage and current settings compared to the Ø(10 cm) W-grid, by a factor of ~10.

Exploratory comparative tests in the same fashion as section 4.2.1 (benchmark, D-load, repeat benchmark again) did not show a significant increase in fusion yield. Combined with the poor initial performance of the grid, further experiments with this setup were abandoned.

4.2.3 Exploratory tests on an icosahedron (ball-shaped) Ti grid

To maximize interaction of fast ions with titanium, a football-shaped grid was constructed from pure titanium mesh-shaped sheet-metal. The resulting grid is shown in Figure 9, and has a diameter of 8.5 cm. The aim of this experiment again was to explore the presence of overly significant increases in neutron yield.

Since this grid's transparency is very low compared to wire grids, star-mode could not be achieved in this configuration. Significant amounts of neutrons were only detected when using the ion-source. After loading the grid with deuterium in a high-pressure plasma (~0.78 Pa) for ~120 minutes, the grid was exposed to the ion beam emanating from the ion source. As a result, only a circular area of approximately 7 cm^2 was exposed to fast ions. The maximum recorded neutron yield in this configuration was recorded at 59.13 kV, 5.60 mA, 0.15 Pa to be $(2.07 \pm 0.45)*10^5$ neutrons/s. Since no star-mode-like discharges could be produced and the strike-area on the grid turned out to be very small, the grid provided no benefits and was discontinued.

4.2.4 Characterizing fusion yield improvements with a solid target

Finally, after determining embedded fusion in the fusor does not increase the neutron yield by extreme amounts, the original titanium target was installed in the titanium grid to characterize the exact (mild) improvement. Unfortunately, the original W grid was lost in an accident during another experiment, making it impossible to further reproduce the most successful measurement from section 4.2.1. The experiment was thus performed with the (small) Ti grid.

With the target mounted inside the grid, the following procedure was performed to verify if and how much embedded fusion contributes over pristine tungsten targets:

1) Initial benchmark measurement of >200s at a stable setting, e.g. <50 kV and <10 mA. One 'low' intensity measurement at 37.5 kV, followed by one 'high' intensity measurement at 43 kV. High intensity benchmark is always performed last, since this heats the grid towards thermal desorption relevant temperatures (faint red glow). Pressure for each benchmark is 0.14 Pa.
2) The titanium target is heat-cycled by operating the fusor at high settings (>50 kV, ~20 mA) until ion-bombardment causes the target to glow white-hot (as observed through the live camera feed), pushing the temperature beyond the thermal desorption temperature (see section 2.3.2). Embedded D is expected to be largely outgassed.
3) Second benchmark measurement. The ion-source is used to fine-tune the plasma current to match the benchmark settings. This step ensures that the pristine target doesn't show different yield numbers after heat-cycling.
4) The target is loaded with deuterium by running a 'high pressure' (0.7 Pa) plasma at low voltage (7.5 kV, 20 mA) for 25 minutes.
5) The benchmark measurement is repeated. Increased fusion yield is expected if embedded fusion contributes.
6) The heat-cycle is repeated, significant outgassing of D out of the target is expected.
7) The benchmark measurement is repeated. Levels of fusion similar to 1) are expected.

The resulting neutron yield during the 4 measurements are plotted in Figure 25. Each step is annotated inside the graph.

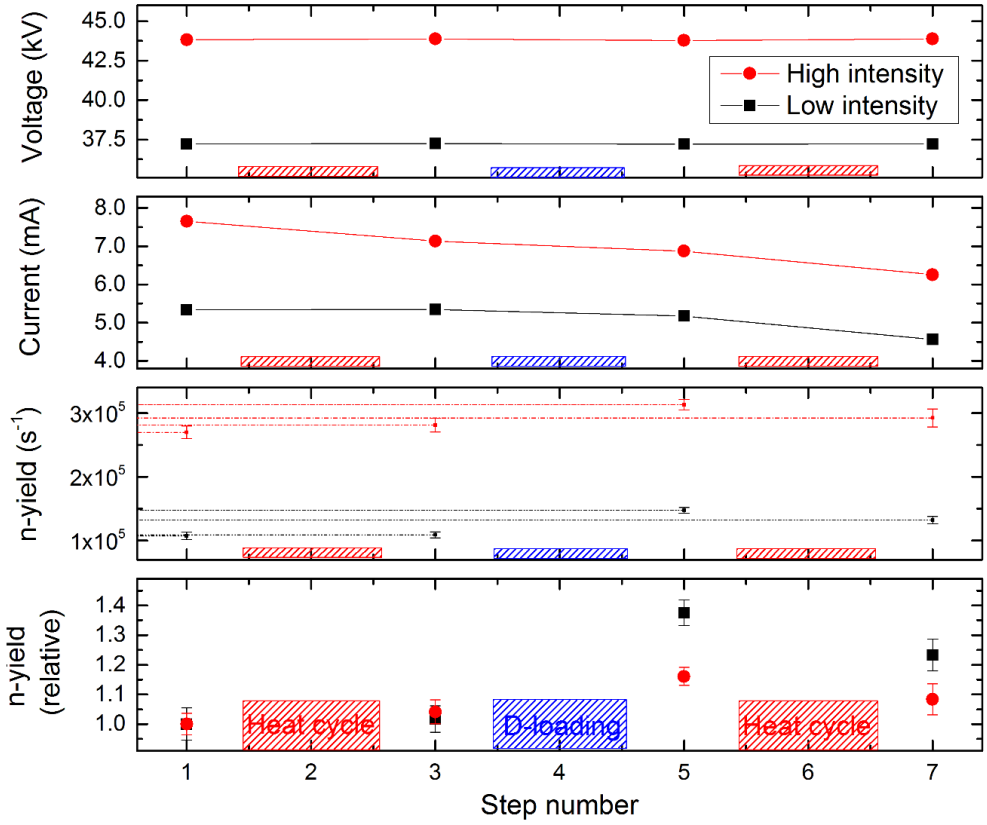

Figure 25: Fusion yield results after running the embedded-fusion procedure for two different voltages (red: 43.8 kV, black: 37.2 kV) at a pressure of 0.14 Pa. The top panel shows the voltage being constant during all measurements. The second panel shows the plasma current, which decreases over the course of the procedure. The bottom two panels show the absolute neutron yield and the relative changes between the shots when normalized to the benchmark. Drop-lines towards the y-axis were added on the third panel for better visibility.

The results show an increase in fusion yield is most prominent in the low-intensity measurement (close to a factor 1.4). The high intensity measurement shows a lower (factor ~1.15) increase. Note that the current is decreasing as the procedure progresses while the voltage and pressure (not plotted) remain constant. The reason of this current drop is unknown, though strengthens the hypothesis that embedded fusion caused the increase in neutron yield since at constant pressure and voltage, a decreasing current is expected to show decreased neutron yield.

It should be noted that the low- and high-intensity benchmarks were performed back-to-back in between the heat-cycle and D-loading phases. Therefore any physical changes of the target caused by the low-intensity shot could have influenced the high-intensity measurement. However, when analyzing the evolution of the neutron yield within the long low-intensity shot, no significant time-dependent changes in yield could be observed.

Note that while the relative yield differs between high- and low intensity, the absolute increase in yield over the non-loaded target are similar the high- and low-intensity discharges: $+3.8*10^4$ and $+3.2*10^4$ additional neutrons/s respectively. Ideally, neutron yields of several orders of magnitude higher were expected. This is further discussed in section 5.2.4.

5 Discussion and conclusions

In this section, results presented in the previous chapter are discussed and loose ends are tied up as much as possible. Where possible, definite conclusions will be drawn. The final paragraph of this chapter will address the research questions posed in section 1.3.

5.1 Fast ion population

5.1.1 Hydrogen and deuterium discharges without ion source

As shown in the results, a simple spectrum of a star-mode plasma yields little quantitative information about the plasma contents and energy distribution. The only numerical value is extracted from the contribution of the stationary plasma in the center, which was not of particular interest to the research questions posed in section 1.3. Note that the error in the obtained value for the ion temperature in the central plasma is high – this is mostly caused by the relatively large error in the determination of the instrumental broadening and the fact that both broadening mechanisms are similar in magnitude. Since the measurements are taken near the physical limits in terms of spectrometer resolution (maximum grating density and the pixel spacing on the CCD camera), this uncertainty could not be avoided, and is amplified during deconvolution of the combined thermal- and instrumental broadening mechanisms. The obtained value of (4.4 ± 1.6) eV for a hydrogen plasma agrees well with values reported by earlier experiments on the TU/e fusor, which indicated 4 eV [10].

The different factors contributing to the shape of the wide broadening profile could not be quantified using this spectrum, partly because of the low resolution. Apart from that, it is not a priori known how many factors should contribute to this shape from a physical standpoint, in terms of the number of contributing species and the factors listed in section 3.2.2. However, qualitatively, since the combination of two Gaussians provides a relatively good envelope fit, it is possible the two Gaussians indicate two distinct dominating populations/species; one being H_2^+ (wide Gaussian) while another unknown species (which is also suspected to contribute in section 4.1.2) is responsible for the 'intermediate' Gaussian (green line in Figure 17). Due to the quality of the source-data leading to the double-Gaussian fit, these results are highly speculative and yield no definite conclusion.

Even though the standard spectrum lacks quantitative information on plasma contents, it is of paramount importance to this thesis, as it is required for comparison to an ion-source driven discharge.

5.1.2 Discharge with ion source – using the ion source as a plasma diagnostic

An attempt was made to solve the complex feature shown in the D-spectrum in Figure 18 by using multiple Gaussian fits. The result is shown in Figure 26. Of particular interest are peaks 2 and 6, which show the peaked behavior of the fast D_2^+ population as identified in section 5.1.2. The fit confirms the presence of a mono-energetic component in the energy distribution of D_2^+, as is expected when injecting ions at the edge of the fusor potential. Peaks 1 and 7 show similar, yet less peaked behavior for D^+, which agrees with the hypothesis that this population is observed in the spectrum through charge-exchange, which can occur anywhere in the vessel. Sattelite peaks 3 and 5 do not fit as these features do not correspond to a species with a mono-energetic energy distribution, indicated by the absence of a definite $\Delta\lambda_{max}$. Therefore this feature is also affected by the factors mentioned in section 3.2.2. As a result, these irregular peaks cannot be fitted with a Gaussian as evident in the plot. While the species contributing to these peaks remain unidentified, it is possible these peaks are caused by H binding to impurities in the plasma. Since the vessel is opened regularly, surface oxidations of the grid could for example introduce oxygen into the vessel. The main suspects for resulting impurities would then be OH, H_2O and H_3O. In future work an effort should be made to identify the origin of these peaks, since the contribution is significant. If caused by contaminations in the plasma, these could harm fusor performance and efforts should be made to avoid them.

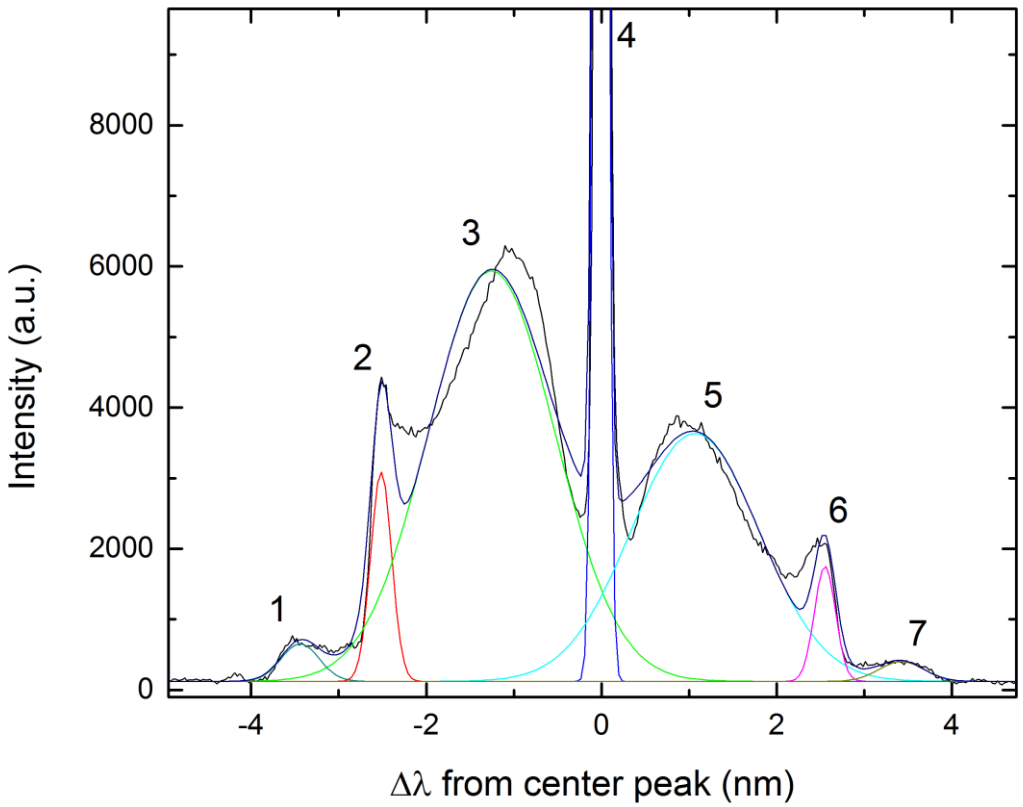

Figure 26: Attempted fit of Doppler-shift profile for a D-plasma injected with a near-mono-energetic ion population.

While not relevant to the research questions, it is interesting to note that the oscillatory motion of ions inside the fusor can be observed through symmetry in shape of the spectrum (Figure 18), since this shows particles traveling in both directions (blue- and red-shifted) while being injected from a single point. The difference in intensity between the red- and blue-shifted parts of the spectrum should not be mistaken as an indicator for diminishing population size between oscillations; since the ions are injected as a beam, the electric field 'confines' this beam during acceleration on the initial pass-through due to the rapid acceleration, while upon deceleration the beam disperses as the positively charged ions repel each other, meaning a fraction of ions move out of the line-of-sight of the spectrometer. This is sketched in Figure 27. In some situations – for instance when operating a different grid or when adjusting the grid position – the symmetry in the spectrum was observed to change significantly or disappear altogether. It is suspected that the alignment of the grid between the ion-source and spectrometer is of high importance, since the grid may deflect or partially block the ion beam.

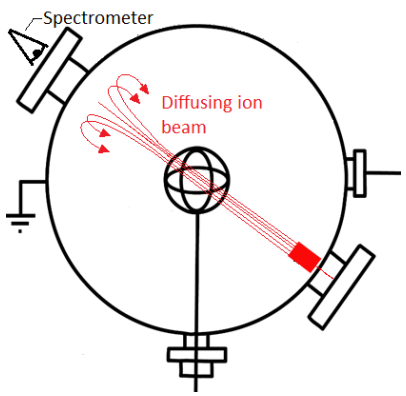

Figure 27: Schematic representation of ion beam diffusion after a single pass-through.

Similarly to section 4.1.1, the ion temperature of the central plasma for an ion-assisted discharge was determined by analyzing the central peak, and turned out to be (4.4 ± 2.2) eV for the hydrogen plasma and (8.8 ± 6.0) eV for the deuterium plasma[2]. The error in the measured peak FWHM is larger compared to the standard star-mode plasma, since the arbitrary shape of the broadening-profile did not allow a sufficiently accurate convoluted fit. For this reason, the fit had to be performed without accurately correcting for the contribution of the broader distribution. Since the intensity of the central peak exceeds the broader distribution by a factor ~10, such fit is an acceptable approximation, but introduces an increased uncertainty in the FWHM. In particular for the deuterium spectrum, the uncertainty turns out to be very big as the Doppler broadening closely nears the instrumental broadening of 0.12 nm.

From the spectra obtained, it has been shown that the fraction of fast ions can be increased significantly by using an edge-mounted ion source compared to a general star-mode plasma. Furthermore, the ion source introduced transient structures ('ridges') and peaks in the broadening profile shown in the spectrum, which allowed for qualitative identification of plasma species. From these spectral features, it was concluded that near-mono-energetic populations of both D_2^+ and D^+ were introduced into the plasma by the ion source and could be monitored by the spectrum. Two large 'shoulder'-like features remain unidentified, but are shown to scale linearly with the discharge voltage in the hydrogen plasma. In the deuterium plasma, $(\Delta\lambda)^2$ plateaus above V_d ~25 kV for unknown reasons. Since these spectral features show no clear transients like the features resulting from the D_2^+ and D^+ populations, no definite conclusions can be drawn on the possible weight of the species causing these 'shoulders'. The same problem arises as discussed earlier, where creating a sensible fit of multiple factors contributing to the resulting shape becomes difficult, thus no hard conclusions can be drawn on their origin. It was hypothesized that contamination by oxygen, either from opening the fusor or from oxidized metals inside the fusor (grid), could contribute to this feature. No adequate supporting evidence or mechanism for this was identified.

An interesting notion to be made is that the edge-mounted ion source – while intended for increasing the fraction of fast ions – doubles as a qualitative plasma probing tool. The ion source ionizes the same source-gas as the main fusor discharge, but deposits the resulting hydrogen-containing species – which differ in mass – mono-energetically into the bulk discharge. Due to the difference in mass, the resulting Doppler-shifted 'transients' (ridges in the spectrum) show up on separate / unique locations in the Doppler-shifted profile, and thus yield information on the plasma composition as opposed to the 'smooth' Doppler-broadening produced in an unassisted star-mode discharge.

5.1.3 Fusion yield scaling – without ion source

In analyzing the operational regime as measured in section 4.1.3, it should be noted that the accessible operational regime and its corresponding neutron yields are specific to the setup used in this thesis. Breakdown characteristics have been observed to change when changes were made to the grid (see sections 4.2.2 and 4.2.3), meaning that using a bigger grid might yield better results in terms of the lowest attainable pressure, as is further detailed in section 6.2. A relatively small grid was used in these experiments out of practicality, such that the grid could be interchanged frequently through one of the auxiliary ports without having to take apart the fusor shell.

5.1.4 Fusion yield behavior - with ion source

One of the research questions addressed whether it is possible to correlate an increase in the fast ion population to an increase in neutron yield. Unfortunately, due to the nature the fusor is operated, clearly showing such correlation proved unsuccessful. For an accurate comparison, the neutron yield should compared between discharges with and without assistance of an ion source, but otherwise identical. Due to the mutual dependencies between voltage, current and pressure, such direct comparison could not be produced, and adding the ion source resulted in a discharge with a higher current and corresponding neutron yield. All pressure regimes yielded difficulties in making an accurate comparison:

- In the high-pressure discharges (where the blue and red datapoints overlap), there are situations where adding the ion-source does not significantly increase the discharge current. While this allows for direct comparison, it is assumed the contribution of the single ion source is negligible compared to the bulk star-mode discharge.
- In moderate pressure discharges, the ion source does significantly contribute to the discharge, but simultaneously increases the discharge current dramatically compared to an unassisted star-mode discharge at the same discharge voltage. Since an increase in current always increases the neutron yield, it is unclear to which extent the altered ion energy distribution contributes and to which extend the increase in current increases the optical emission of the plasma such that the intensity of spectral features can be accurately compared.

- In low-pressure discharges (where the highest neutron yields were achieved), a comparative star-mode discharge could not be produced at all.

While in all cases with $p < 0.26$ Pa it has been shown that adding the ion source increased the neutron yield, with a maximum achieved increase of ~3x compared to the best unassisted star-mode discharge, the spectral data collected in this research draws no conclusion on the effect of the increased fast ion population.

In moderate pressure discharges, it could be possible to normalize the different spectra obtained from unassisted and assisted star-mode by the difference in current at the same voltage. However, this requires an accurate characterization of the effect of current increase *without ion source* while the pressure and voltage are kept constant. As evident from the results, such analysis cannot be made since the voltage and current cannot be changed independently for a star-mode discharge.

A final notion to be made is that in this thesis, due to the geometrical setup of the source and spectrometer (opposite to each other), the increase in intensity of certain spectral features cannot be assumed to be representative for the entire plasma. The measured effects on the Doppler-broadening are only valid in a single direction. The measurements cannot be expanded as being representative for the entire discharge on grounds of symmetry, since the assisted discharge is no longer spherically symmetric.

5.1.5 Comparing data to the neutron yield model

Throughout this thesis, an attempt was made to correlate the increase in fast ions to an increase in neutron yield, by correlating spectral features to neutron yields of various discharges. While an increased fast ion population was shown, it could not be quantified due to the nature of the fusor setup (varying current and resulting discharge intensity) and the geometry of the compared discharges (star-mode vs. single beam). Using the simple scaling model proposed in section 2.3.3, an attempt can be made to characterize the effect of the ion source on neutron yield by investigating how the various datasets compare to values predicted by the model. The model assumes mono-energetic ions, so it is hypothesized that the experiments with the ion source are more in line with the model, while the experiments without the source (having a larger spread in ion energy) will yield a lower than predicted neutron yield.

Using the voltage, current and pressure of all data-points in Figure 24 (see Table 2 in Appendix A), the predicted neutron yield was calculated for every individual measurement. A plot of predicted vs. measured neutron yield was made and is shown in Figure 28. Reasonably good agreement can be observed between the model and resulting values, as well as clear differences between the different data-sets. Note that a steeper trend indicates 'better than expected' performance according to the model. It is tempting to conclude that the discharges purely driven by the ion source produced higher neutron yields due to the increased fast ion fraction. However, it should be noted that the better performing data-points were coincidentally produced at lower pressures, thus concluding the fast ion fraction is the driving effect would be premature. As mentioned in section 2.3.3, the effect of recycling was not taken into account when deriving the model. Without knowing the exact dynamics, the scaling model can still be adapted to include the scaling of recycling, foregoing the ability to predict exact neutron yield numbers.

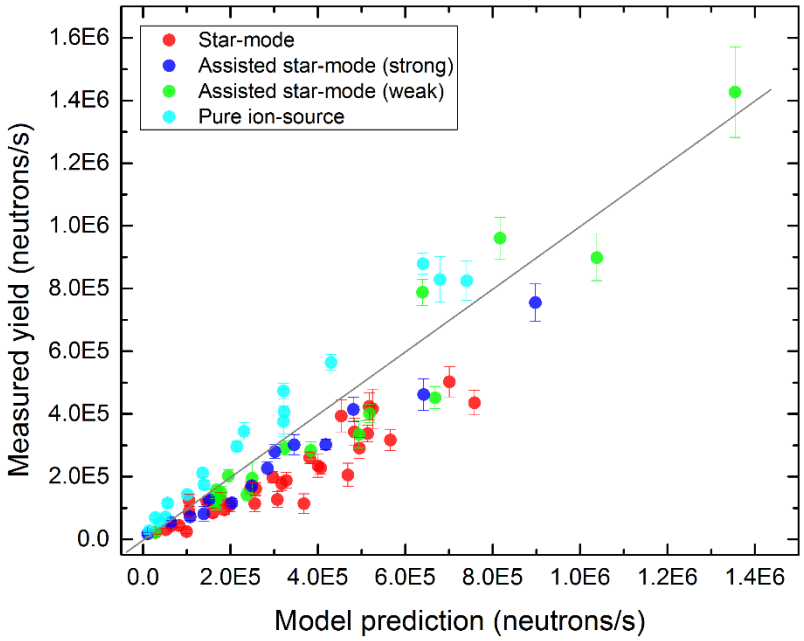

Figure 28: Scatterplot showing model-predicted vs. measured neutron yield for all datapoints of Figure 24, color-coded accordingly. The grey line indicates the 1:1 baseline. The different groupings show varying performance compared to the model, with the purely ion-source driven shots performing best and regular star-mode performing the worst.

This correction can be made qualitatively. The number of oscillations an ion makes can in essence be interpreted as a multiplier for the beam-length *d* (see formula (9)). Assuming the number of oscillations an ion can make through the grid (neglecting grid losses) is limited by the mean-free-path, this number should scale inversely with pressure, assuming the cross-section for this loss-process is roughly constant. Dividing formula (10) by the pressure and repeating the process above yields the scatterplot shown in Figure 29.

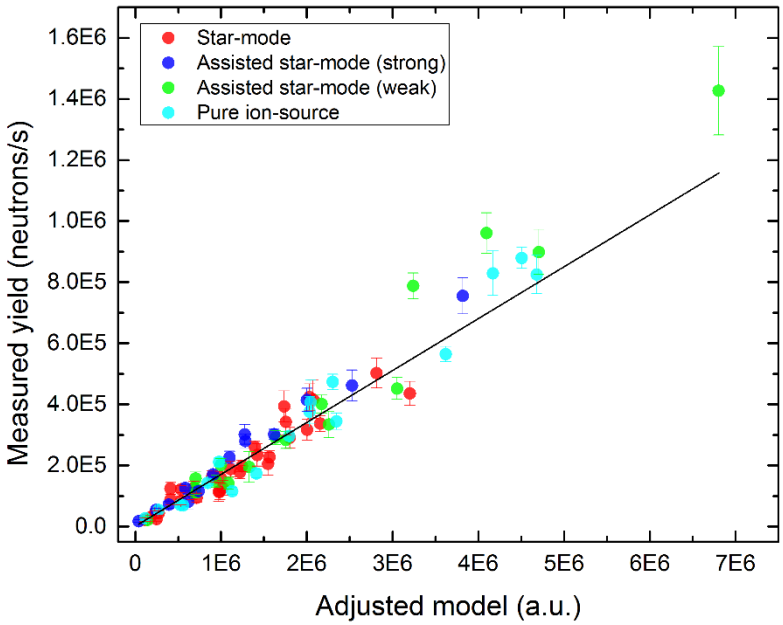

Figure 29: Scatterplot in the same fashion as Figure 28, with the model adjusted to qualitatively incorporate the effect pressure has on ion recycling. No clear difference between datasets can be observed anymore, indicating ion recycling effects cannot be neglected. The y-axis contains arbitrary numbers since only the scaling of recycling is incorporated. The straight line indicates a linear fit through all data-points.

The resulting plot shows good agreement with the scaling of the model across almost all data-points. Therefore it cannot be concluded that the increased fast ion fraction provides a significant increase in neutron yield from this data. It is possible that the overall contribution of the ion-source is still small compared to other ionization mechanisms.

From the data shown in Figure 29 it is possible to derive an empirical scaling law for the bulk of the range investigated. Using the linear fit, a scaling factor was derived for the lower end of the fusor:

$$Neutron\ yield[\frac{neutrons}{s}] = 1.42 * 10^{35} * I_{fusor}[mA] * \sigma\left(0.5 * eV_{fusor}\right)[m^2] \quad (24)$$

The scaling law does not agree well with the high neutron-yield shots at low pressure, as these data-points outperform the model. It could be possible that at low enough pressure, ion-ion interactions start becoming significant.

5.2 Deuterium loaded target

5.2.1 Exploratory test results on Ti target inside W grid

Since the W grid was lost in an accident during a different experiment on the fusor, it was not possible to reproduce the effects observed during the test run. The data recorded during this test-run could not be used as the discharge parameters V_d and I differed between the shots. Since the solid target blocks some of the discharge, the current did not match and while V_0 was kept constant between the shots, due to the varying currents a varying voltage drop over the balance resistor yielded different V_d between shots.

5.2.2 Exploratory tests on a small Ti grid

The most notable effect from using the smaller Ti grid was a significant decrease in neutron yield, by a factor of ~10 compared to the W grid. The thickness of the grid-wires and the decrease of the volume inside the grid are believed to be the main cause. Since the Ti grid uses 2 mm wire-thickness instead of the 0.44 mm wire used in the W grid, ion-grid interactions are expected to be more dominant – effectively the grid transparency is reduced. This choice was intentional, as the effects of deuterium-loading of the grid wires was expected to be very significant in the ideal case.

The decreased grid-size is believed to be the main cause of the decreased neutron yield. As the ions travel at maximum velocity within the grid (*E=0)*, decreasing this volume decreases the total interaction time of the ions with the background gas when the fusion cross-section is highest. This will decrease neutron yield, hence a larger grid is expected to perform better (see section 6.2).

5.2.3 Exploratory tests on an icosahedron (ball-shaped) Ti grid

Interaction between the grid and plasma turned out to be no better than using a solid Ti target and a stable discharge could not be maintained long enough to yield proper measurements, except at high pressure where neutron yields were inherently low. The low transparency of the grid inhibits the plasma from stably igniting at low pressures, and greatly decreases the resulting plasma current and corresponding neutron yield.

Moreover, due to the small cross-sectional area that faces the discharge, the strike-point on the grid behaved like a hot-spot that heats up rapidly, turning white-hot within several seconds. At that point the deuterium is lost from the grid and vessel pressure could not be maintained stable. A ball-shaped grid was deemed unsuited for steady-state operation in this configuration.

5.2.4 Characterizing fusion yield improvements with a solid target

The obtained neutron yields can be compared to similar discharges where no target was used. For the low power discharge (37.2 kV, 5.3 mA, 0.14 Pa) ~$1.5*10^5$ n/s were measured, compared to $2.11*10^5$ n/s for a similar discharge (37.2 kV, 5.4 mA, 0.14 Pa) without target. Similarly, ~$3.1*10^5$ n/s were measured in the high power discharge (43.8 kV, 7.6 mA, 0.14 Pa) with target, compared to ~$4.7*10^5$ n/s for a similar (43.8 kV, 7.75 mA, 0.14 Pa) discharge without target. This can be explained by the target blocking the ion beam, thus affecting ion recycling. In future applications, embedded fusion should be utilized in a way that does not interfere with the central plasma.

After characterizing the effect of embedded fusion on an intra-grid mounted solid target, the effect on neutron yield turned out to be mild (40% in the best recorded case) compared to the expectation based on the factor 10^3 increase in total deuterium. This could be explained by (a combination of) the following:

- Fast deuterium ions are far more likely to scatter and lose energy to the Ti atoms, greatly reducing the fusion cross-section. Since Ti-atoms are much larger than D-atoms embedded in the lattice, this is a reasonable assumption.
- The titanium is not adequately loaded with D after an hour of loading. Since ion flux numbers in the fusor at appropriate energies (>1 keV/D^+) are not exactly known a priori, resulting deuterium content is hard to predict besides the back-of-the-envelope model presented in Appendix B. Measurements using pre-loaded targets and varying loading times for in-situ loading could be performed in the future to characterize the effects (see section 6.2).

Note that the relative change in neutron yield can be roughly described using formula (4):

$$\frac{Vn_i n_g \langle \sigma v \rangle_{gas,2} + Adn_i n_t^D \langle \sigma v \rangle_{target,2}}{Vn_i n_g \langle \sigma v \rangle_{gas,1} + Adn_i n_t^D \langle \sigma v \rangle_{target,1}} = Yield - factor$$

where V is the volume inside the grid, n_i the ion density, n_g the gas density, n_t^D the deuterium density in the target, A the target area, d the thickness of the D-layer in the T, $<\sigma v>_{target}$ the fusion reaction rate for embedded fusion and $<\sigma v>_{gas}$ the fusion reaction rate between free particles. Subscripts "1" and "2" indicate "before" and "after" D-loading respectively. Note that n_i can be considered equal for all shots, $n_t^D = 0$ before D-loading the target and $<\sigma v>_{gas,1} = <\sigma v>_{gas,2}$ since the 'before' and 'after' discharge are equal in terms of voltage. The formula above simplifies to

$$\frac{Vn_g \langle \sigma v \rangle_{gas} + Adn_t^D \langle \sigma v \rangle_{target}}{Vn_g \langle \sigma v \rangle_{gas}} = Yield - factor$$

Since V, n_g, and A and d are known, the factor $n_t^D \langle \sigma v \rangle_{target}$ can be expressed in terms of $\langle \sigma v \rangle_{gas}$ which allows a comparison to be made between the effectivity of both mechanisms. The results indicate that either n_t^D is much lower than expected by the calculation in Appendix B, or that the embedded-fusion reaction rate $\langle \sigma v \rangle_{target}$ is a lot smaller in solid Ti. This could be explained by scattering effects of the light D-nuclei with the heavy Ti. With scattering effects dominating, a fast D ion will lose most of its energy before reaching a D, resulting in a lower reaction rate. The results also indicate $n_t^D \langle \sigma v \rangle_{target}$ does not scale strongly to the discharge voltage, contrasting $\langle \sigma v \rangle_{gas}$.

In all cases, grid/target temperature is a real problem, since outgassing of deuterium content can occur as early as 350 K [17]. Without adequate cooling, target-based embedded fusion is not expected to be useful for long-term steady-state operation, since grid and targets glow white-hot at the most intense settings of the fusor.

5.3 Overall conclusion and answers to the research questions

Spectroscopy has been demonstrated as a successful diagnostic on the fusor. For a star-mode discharge, ion energies of (4.4 ± 1.6) eV were observed for a hydrogen plasma, while ion-source assisted discharges yielded (4.4 ± 2.2) eV for hydrogen and (8.8 ± 6.0) eV for deuterium. The Doppler-shifted profiles observed in the ion-source assisted discharges allowed individual plasma species and their maximum kinetic energy to be identified, showing both the presence of D^+ and D_2^+ at ion energies close to $E_{kin,max}$ for discharges of varying voltage. The additional 'shoulder'-like feature could not be identified as a definite species with acceptable certainty, and can be a combination of several species with an unknown ion energy distribution.

It is now possible to answer the research questions posed in section 1.3.

Starting with **Q. 1**, it has been shown that the fast ion population can indeed be artificially increased compared to a regular star-mode discharge by using an ion-source mounted on the edge of the vessel. The relatively small source significantly alters the energy distribution as deduced from spectroscopic measurements, showing significant increases in optical emission for species close to their maximum theoretically possible kinetic energy.

Use of the ion source enabled a clear extension to previously unattainable low-pressure regime, yielding a significant increase in neutron yield (**Q. 1**) over a regular star-mode discharge with a maximum recorded neutron yield of $(1.43 \pm 0.14)*10^6$ s^{-1}. However, an exact correlation between the increased fast ion density and increase in neutron yield cannot be made for two reasons:

- Discharge parameters in terms of V_d and I cannot be reproduced between an unassisted and assisted discharge as these cannot be varied independently

- The spectrum does not represent the ion energy distribution of the entire plasma, since asymmetry is expected due to the single injection point of fast ions.

In an attempt to test the effectiveness of injecting a mono-energetic ion population in the fusor, a simple back-of-the-envelope model was derived from physical arguments where discharges with the ion source were expected to perform better (when compared to the model) than a star-mode discharge. Taking into account recycling as a pressure-dependent parameter, this could not be demonstrated. Surprisingly, the data fitted the model rather well, resulting in an empirical scaling law for the TU/e fusor that depends only on voltage and current. Using this scaling law, an attempt can be made to answer **Q. 3**, by inserting the maximum voltage and current the PSU can deliver. At 120kV and 100 mA, this results in a maximum neutron yield of $3.01*10^7$ neutrons/s for the current situation. However, since the fit is dominated by the data-points in the lower end bulk, it is assumed that this scaling law describes the potential of regular star-mode operation in the current fusor configuration. Note that the best ion-assisted shots acquired in this work outperform the empirical scaling law considerably on the high end. Further improvements on the central grid and ion energy distribution are expected to significantly increase the potential maximum neutron yield of the TU/e fusor.

Deuterium loading experiments showed a moderate increase in neutron yield can be demonstrated in a deuterium-loaded Ti target compared to a non-loaded Ti target (**Q. 2**), however the act of inserting a target decreased the neutron yield due to partial blockage of the discharge (**Q. 2**). While the resulting 'embedded fusion' is plausible as a fusion mechanism, this has to be incorporated in the overall setup in a way that does not interfere with the plasma (see section 6.2).

Since the maximum recorded neutron yield in this thesis is $(1.43 \pm 0.14)*10^6$ neutrons/s, the target yield of 10^9 s^{-1} could not be achieved by the configuration used in this thesis (**Q. 3**). However, the results presented in this thesis indicate a clear path to further optimizations that expand on the mechanisms researched in **Q. 1** and **Q. 2**. In this work the optimizations were not fully utilized, hence the answer to **Q. 3** remains as of yet undefined. Future design considerations that should fully utilize these optimizations – and thus possibly reach 10^9 neutrons/s – are discussed in the next and final chapter.

6 Outlook

6.1 Expanding on the ion source

As was made clear from the results especially in section 4.1.4, using an ion source mounted at the edge of the vessel significantly expands the operational regime towards the low-pressure end. Where during normal star-mode operations discharge current, grid longevity and overall stability limits the maximum neutron yield, in regimes assisted by an ion source significantly higher neutron yields can be achieved with lower strain on the grid and power supply. This resulted in a neutron yield that was limited by the maximum ion current output of the ion source. Evidently, significant improvements are expected if the discharge current can be increased in the low-pressure regime. Adding additional ion sources could be one solution, however the setup is inherently limited by the auxiliary ports, which moreover are mostly in use for diagnostics.

Therefore a novel multi-grid configuration is proposed. The ion source is in essence simply an anode and cathode spaced close enough together (~ 1 mm) such that a low voltage of 1 kV yields an electric field strong enough to form a discharge even at very low pressure. The electrons are lost to the anode while the ions are ejected. Consequentially, it is possible to convert the entire fusor wall into an ion source, a proposal of which is sketched in Figure 30.

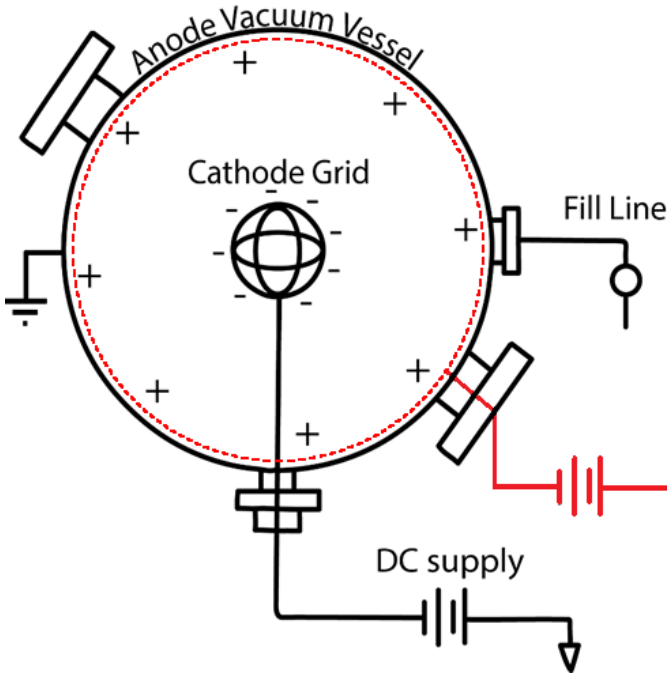

Figure 30: Proposal for multi-gridded fusor configuration, utilizing a large intermediate grid placed very close to the vessel wall. When a small (~1 kV) potential difference is realized between the vessel wall and intermediate grid, the entire region acts as an ion source, ejecting ions towards the central cathode.

A secondary 'intermediate' mesh-grid is constructed and positioned very close to the vessel wall (several mm). This way the entire vessel wall can act as an ion source, which should provide ample ion current to maximize the neutron yield under low pressure settings. Since the intermediate grid is positioned very close to the wall, a low potential difference will be sufficient to create a discharge between the grid and vessel wall. The ions will then be accelerated towards the central region and experience the full -60kV potential drop towards the cathode. Summarized, the benefits of such design compared to a conventional configuration are:

- The fusor can be operated at extremely low pressures, which was shown to be beneficial for neutron yield
- Since ionization only occurs at the edge of the vessel, all ions will be accelerated by the full vacuum-potential. At extremely low pressure, ion formation near the grid can be minimized.

The ion energy distribution in the center should be peaked around $\sim eV_0$ with V_o the cathode voltage.

- At low enough pressure, ion-ion interactions may start dominating over ion-gas, such that fusion yield starts scaling with I^2.
- Better control over the discharge is gained, both in terms of stabilization and in terms of fine-tuning, as the current-control between the intermediate grid and the vessel wall can be used to determine the amount of ions to be created

The resulting expected electric potential and corresponding electric field strength are plotted in Figure 31. Note the spike in electric field strength in the region between the intermediate grid and the wall.

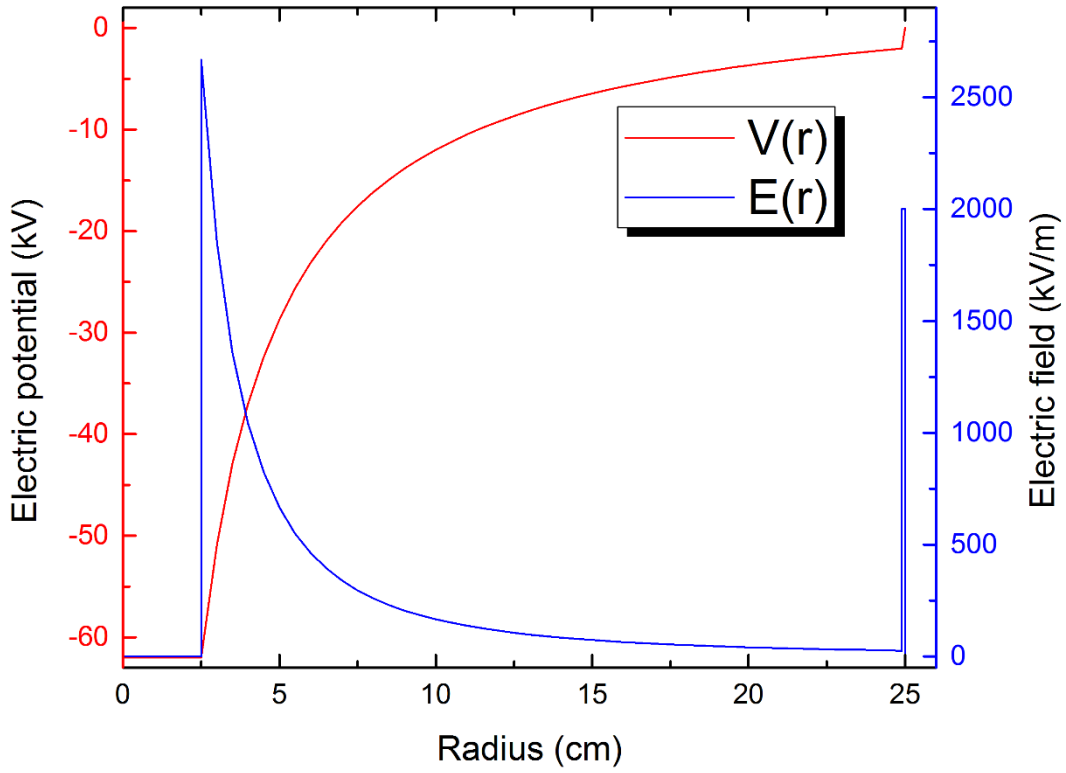

Figure 31: Sketch of expected electric field strength and electric potential expected when using the Huisman-configuration.

An appropriate scheme will need to be designed for the power supply configuration, such that the voltages of the cathode and intermediate grid can be adjusted individually.

6.2 Embedded fusion and cathode-grid considerations

As embedded fusion did show an increase in fusion yield in specific cases, this might still be an interesting avenue of exploration. The effect could be better characterized with the use of ex-situ pre-loaded targets with known deuterium content. Alternatively, measurement series could be performed on targets exposed to deuterium loading shots of varying intensity and duration to characterize ideal loading conditions.

Since the use of a target inside the grid decreased the neutron yield due to partial plasma blockage, embedded fusion should be exploited in non-intrusive ways such that the discharge is not affected. For instance, the vessel wall could be coated with a deuterium-retaining metal such that fast ions lost from confinement through charge-exchange retain a non-zero probability of fusing with the deuterium embedded in the wall.

As interaction with the cathode grid can never be completely avoided, an optimized grid out of D-retaining metal could be constructed. Since ideally the benefits of embedded fusion should provide an increase in neuton yield in steady-state, it is important grid-temperatures do not exceed the thermal desorption temperature limit as mentioned in section 2.3.2. To this end, a water-cooled grid could be

constructed to avoid outgassing during high power operations. Viability of a water-cooled grid has been demonstrated before by A. Seltzman [28].

Additionally, a water-cooled grid might prove beneficial in conjunction with the proposed multi-grid-configuration, since this reduces thermionic emission at the grid – and thus reduces creation of slow ions near the grid – as the cathode grid heats up from ion bombardment.

The grid size and construction should also be optimized to maximize neutron yields:

1) Using a larger central grid, the volume in which the ions travel at maximum kinetic energy is increased. The ions will have a longer interaction-time with the background gas when at this maximum velocity (within the grid, their kinetic energy does not change as $E=0$) compared to a small grid, which should thus increase the neutron yield.
2) A sweet-spot in grid-size and wire-thickness should be determined for regular star-mode operation (unassisted by an ion source) to allow operation at lower pressure. Intuitively, larger would seem better since the cathode and anode are effectively closer together, benefitting plasma breakdown at lower pressures. However, due to the spherical geometry, the electric field strength at the grid is higher for *small* grids, which is important since the driving mechanism for breakdown is field emission. In a large grid this can be compensated for with thinner grid-wires to increase the local electric field directly at the wire.

However, a big drawback of using a larger grid is that it cannot be changed easily afterwards due to the diameter of the auxiliary ports. A grid of the same diameter as the largest access port of the fusor (the port for the electric feedthrough) may be most practical.

6.3 Stability and optimization of HV-setup

As mentioned in section 3.4, the fusor is in some cases limited by instabilities occurring when above a certain voltage, generally 60kV. The largest issues are the resulting disturbance of the neutron detectors (no measurements can be performed) and physical instability of the setup in terms of a swinging grid. It is hypothesized that sparking could cause spikes in EM radiation and cause the grid to swing. Unless the cause of these issues is identified and resolved, voltages higher than 60kV cannot be stably achieved.

Finally, experiments varying the resistance of the ballast resistor can be performed in an attempt to gain more control over the fusor discharge. As discussed, in the current configuration no measurement series can be performed in which either V_d or I is kept constant, making it difficult to characterize the direct influence of the current and voltage. Since V_d depends on the voltage drop over the ballast resistor caused by the current, varying resistance of the ballast resistor may enable an operator keep V_d constant between shots of varying I.

7 Literature

[1] A. S. Eddington, *The Internal Constitution of the Stars*. 1926.

[2] https://www.iter.org/proj/inafewlines, "About ITER." .

[3] R. L. Hirsch, "Inertial-Electrostatic Confinement of Ionized Fusion Gases," *J. Appl. Phys.*, vol. 38, no. 11, pp. 4522–4534, Oct. 1967.

[4] G. L. Kulcinski *et al.*, "Alternate applications of fusion-production of radioisotopes," *Fusion Sci. Technol.*, vol. 44, no. 2, pp. 559–563, 2003.

[5] G. H. Miley and S. K. Murali, *Inertial Electrostatic Confinement (IEC) Fusion*. New York, NY: Springer New York, 2014.

[6] J. P. Freidberg, *Plasma physics and fusion energy*, vol. 1. 2007.

[7] P. T. Farnsworth, "Electric discharge device for producing interaction between Nuclei," US3258402, 1966.

[8] N. A. Krall, "The Polywell: A Spherically Convergent Ion Focus Concept," *Fusion Technol.*, vol. 22, p. 9, 1992.

[9] Y. G. Y. Gu, P. Heck, and G. Miley, "Ion focus via microchannels in spherical inertial-electrostatic confinement and its pulsed experiment results," *Int. Conf. Plasma Sci. (papers Summ. form only Receiv.*, 1995.

[10] A. J. Wolf, "Measurement of ion velocities in the TU/e Fusor plasma using LIF spectroscopy," Eindhoven University of Technology, 2015.

[11] D. B. Go and D. A. Pohlman, "A mathematical model of the modified Paschen's curve for breakdown in microscale gaps," *J. Appl. Phys.*, vol. 107, no. 10, 2010.

[12] W. Hwang, Y. -K. Kim, and M. E. Rudd, "New model for electron-impact ionization cross sections of molecules," *J. Chem. Phys.*, vol. 104, no. 8, pp. 2956–2966, Feb. 1996.

[13] G. M. McCracken and J. H. C. Maple, "The trapping of hydrogen ions in molybdenum, titanium, tantalum and zirconium," *Br. J. Appl. Phys.*, vol. 18, no. 7, pp. 919–930, 1967.

[14] J. Bohdansky, J. Roth, M. K. Sinha, and W. Ottenberger, "Trapping coefficients of energetic hydrogen (0.3-8 keV) in Ti at high doses," *J. Nucl. Mater.*, vol. 63, pp. 115–119, 1976.

[15] J. Roth, W. Eckstein, and J. Bohdansky, "DEPTH PROFILING OF D IMPLANTED INTO Ti AT DIFFERENT TEMPERATURES.," *Radiat. Eff.*, vol. 48, no. 1–4, 1978.

[16] A. E. Pontau, K. L. Wilson, F. Greulich, and L. G. Haggmark, "The nucleation and growth of TiD2 in deuterium-implanted titanium," *J. Nucl. Mater.*, vol. 91, no. 2–3, pp. 343–346, Jul. 1980.

[17] W. Lisowski, E. G. Keim, Z. Kaszkur, and M. A. Smithers, "Decomposition of thin titanium deuteride films; thermal desorption kinetics studies combined with microstructure analysis," *Appl. Surf. Sci.*, vol. 254, no. 9, pp. 2629–2637, 2008.

[18] H.-S. Bosch and G. . Hale, "Improved formulas for fusion cross-sections and thermal reactivities," *Nucl. Fusion*, vol. 33, no. 12, pp. 1919–1919, 2002.

[19] M. A. Gigosos and V. Cardeñoso, "New plasma diagnosis tables of hydrogen Stark broadening including ion dynamics," *J. Phys. B At. Mol. Opt. Phys.*, vol. 29, pp. 4795–4838, 1996.

[20] V. A. Ankudinov, S. V. Bobashev, and E. P. Andreev, "Measurement of lifetimes of excited states of the hydrogen atom," *J. Exp. Theor. Phys.*, vol. 21, no. 1, pp. 26–32, 1965.

[21] H.-J. Kunze, *Introduction to Plasma Spectroscopy*, vol. 56. Berlin, Heidelberg: Springer Berlin Heidelberg, 2009.

[22] H. D. Young and R. A. Freedman, *University Physics*. 2010.

[23] A. Seltzman, "Anode layer ion source (design and specifications)," 2017. [Online]. Available: http://www.rtftechnologies.org/physics/anode-layer-ion-source.html.

[24] P. M. Stier and C. F. Barnett, "Charge exchange cross sections of hydrogen ions in gases," *Phys. Rev.*, vol. 103, no. 4, pp. 896–907, 1956.

[25] G. Karlsson, “User manual: Studsvik Neutron Dose Rate Meter 2202 D.” 1973.

[26] H. Tawara, Y. Itikawa, H. Nishimura, and M. Yoshino, “Cross Sections and Related Data for Electron Collisions with Hydrogen Molecules and Molecular Ions,” *Journal of Physical and Chemical Reference Data*, vol. 19, no. 3. pp. 617–636, 1990.

[27] T. TABATA and T. SHIRAI, “Analytic Cross Sections for Collisions of H+, H2+, H3+, H, H2, and H− With Hydrogen Molecules,” *At. Data Nucl. Data Tables*, vol. 76, no. 1, pp. 1–25, 2000.

[28] A. Seltzman, “IEC Fusion Reactor Mark 3 Fluorinert Cooled Grid,” 2007. [Online]. Available: http://rtftechnologies.org/physics/fusor-mark3-cooled-grid.htm.

Appendix A: Error analyses and full data-sets

Error analysis for instrumental broadening deconvolution and conversion to eV.

Calculating the error in the average ion temperature of the central peak of a measured spectrum is a two step process. First, the measured peak is deconvoluted using formula (21), where an additional error is introduced. The error of the resulting $\Delta\lambda_{FWHM}^{Doppler}$ is calculated by

$$\Delta_{\Delta\lambda_{FWHM}^{Doppler}} = \left| \frac{2\,\Delta\lambda_{FWHM}^{total}}{\sqrt{(\Delta\lambda_{FWHM}^{total})^2 - (\Delta\lambda_{FWHM}^{Instr.})^2}} \right| \Delta_{\Delta\lambda_{1/2}^{total}} + \left| \frac{-2\,\Delta\lambda_{FWHM}^{Instr.}}{\sqrt{(\Delta\lambda_{FWHM}^{total})^2 - (\Delta\lambda_{FWHM}^{Instr.})^2}} \right| \Delta_{\Delta\lambda_{FWHM}^{Instr.}}$$

After converting formula (14) to yield the temperature in eV, the error in this temperature is calculated by

$$\Delta_{T_{eV}} = \Delta_{\left(\frac{k_B T}{e}\right)} = \left| \frac{2 * \Delta\lambda_{FWHM}^{Doppler} * mc^2}{8 * \ln(2) * e} \left(\frac{1}{\lambda_0}\right)^2 \right| \Delta_{\Delta\lambda_{FWHM}^{Doppler}}$$

Neutron yield experiments

The error in neutron yield was calculated in terms of 68% intervals, since counting neutrons for a determined period of time is Poisson-distributed in nature. For a measurement of *x* seconds, the total number of counts yields 68% interval of $\sqrt{counts}$. Both are divided by the total measurement time *x* resulting in counts per second, or *cps*. This error is random in nature.

The *cps* is then converted to total neutron yield in neutrons/s by formula (23), which introduces an additional non-random systematical error of 6.8%. In comparing measurements to each other, this 6.8% can be ignored, while the 68% interval cannot. The raw data of all data-points of Figure 24 and their corresponding neutron yields and error intervals is listed in Table 2, sorted by neutron yield.

Table 2: Raw data corresponding to Figure 22 and Figure 23 in section 4.1. Calculated neutron yields and their errors are listed. Entries are color-coded according to the color-coding used in the 3D scatterplot.

Voltage (kV, avg)	Current (mA, avg)	Pressure (Pa, avg)	CPS	Δ_{CPS} (68%)	n-Yield (neutr./s)	$\Delta_{n\text{-}yield}$ (68%)	Δ_{sys}	Total error
13.36	65.60	0.495	0.138	0.098	**9125**	6452	620	7073
10.36	35.10	0.493	0.160	0.056	**10564**	3735	718	4453
11.84	48.70	0.497	0.192	0.079	**12722**	5194	865	6059
16.94	4.04	0.259	0.258	0.065	**17100**	4275	1163	5438
27.97	1.95	0.195	0.319	0.130	**21114**	8620	1436	10055
21.48	4.01	0.259	0.331	0.088	**21896**	5852	1489	7341
14.06	57.34	0.402	0.368	0.111	**24338**	7338	1655	8993
26.53	1.92	0.119	0.401	0.076	**26538**	4881	1805	6685
17.58	14.46	0.299	0.453	0.079	**29988**	5220	2039	7259
20.52	9.91	0.279	0.653	0.102	**43191**	6745	2937	9682
18.24	19.18	0.298	0.661	0.100	**43707**	6589	2972	9561
20.08	11.39	0.258	0.814	0.089	**53833**	5909	3661	9570
29.68	3.06	0.140	0.819	0.101	**54172**	6489	3684	10173
15.11	86.64	0.488	0.968	0.395	**64022**	26137	4353	30490

45.04	1.74	0.050	1.041	0.103	**68899**	6607	4685	11292
35.34	3.37	0.100	1.071	0.120	**70850**	7709	4818	12526
19.73	19.69	0.275	1.078	0.170	**71327**	11278	4850	16128
25.88	11.11	0.225	1.224	0.353	**81007**	23385	5508	28893
19.35	29.12	0.297	1.268	0.211	**83860**	13977	5702	19679
22.95	11.40	0.256	1.330	0.266	**87973**	17595	5982	23577
23.12	19.33	0.259	1.418	0.224	**93838**	14837	6381	21218
19.57	34.44	0.299	1.635	0.321	**108180**	21216	7356	28572
28.04	9.53	0.238	1.688	0.267	**111656**	17654	7593	25247
23.65	24.46	0.259	1.709	0.382	**113087**	25287	7690	32977
17.14	88.74	0.378	1.711	0.474	**113162**	31385	7695	39080
54.18	1.99	0.050	1.746	0.172	**115493**	11074	7854	18928
20.98	28.96	0.274	1.753	0.190	**115944**	12576	7884	20460
21.33	19.57	0.273	1.834	0.178	**121324**	11784	8250	20034
28.04	9.54	0.238	1.864	0.281	**123342**	18594	8387	26982
22.98	11.36	0.255	1.881	0.294	**124422**	19431	8461	27892
21.77	19.80	0.258	1.904	0.138	**125980**	9116	8567	17682
22.83	19.36	0.260	1.905	0.337	**126011**	22276	8569	30845
20.16	46.73	0.302	1.912	0.375	**126475**	24804	8600	33404
28.25	14.41	0.219	2.134	0.290	**141203**	19215	9602	28817
37.85	4.43	0.120	2.156	0.151	**142608**	9693	9697	19390
38.75	4.60	0.189	2.249	0.301	**148785**	19882	10117	30000
28.07	9.56	0.238	2.377	0.312	**157256**	20649	10693	31342
23.68	24.50	0.259	2.428	0.297	**160596**	19620	10921	30540
22.05	28.97	0.274	2.466	0.289	**163155**	19096	11095	30190
21.42	32.82	0.274	2.579	0.152	**170610**	10088	11601	21690
44.51	4.55	0.099	2.626	0.217	**173719**	13991	11813	25804
23.93	28.98	0.260	2.683	0.330	**177492**	21848	12069	33917
20.39	48.77	0.294	2.836	0.376	**187607**	24849	12757	37606
33.94	9.73	0.188	2.941	0.759	**194576**	50239	13231	63471
26.92	19.43	0.239	2.982	0.273	**197307**	18087	13417	31504
36.83	5.69	0.196	3.048	0.311	**201618**	20578	13710	34288
20.66	64.39	0.303	3.100	0.557	**205084**	36834	13946	50780
37.21	5.39	0.140	3.194	0.222	**211332**	14294	14371	28665
23.06	29.95	0.259	3.416	0.307	**225987**	20294	15367	35661
24.49	34.21	0.259	3.436	0.310	**227296**	20495	15456	35951
22.07	45.71	0.282	3.534	0.552	**233827**	36518	15900	52418
22.96	38.65	0.273	3.922	0.284	**259462**	18774	17643	36417

27.33	19.07	0.234	4.227	0.330	**279628**	21835	19015	40850
32.49	14.75	0.219	4.274	0.421	**282741**	27859	19226	47086
23.12	48.64	0.274	4.393	0.504	**290628**	33337	19763	53100
36.80	9.35	0.198	4.395	0.340	**290738**	22498	19770	42268
44.29	5.86	0.120	4.476	0.241	**296119**	15492	20136	35628
22.51	38.11	0.270	4.555	0.488	**301339**	32307	20491	52798
24.00	38.09	0.258	4.564	0.239	**301909**	15781	20530	36311
22.69	57.98	0.282	4.780	0.512	**316240**	33905	21504	55409
32.23	19.47	0.219	5.043	0.657	**333607**	43432	22685	66117
28.11	29.12	0.238	5.090	0.390	**336722**	25825	22897	48723
23.01	48.23	0.275	5.169	0.662	**341993**	43788	23256	67043
50.05	5.29	0.098	5.205	0.422	**344374**	27183	23417	50600
38.97	9.75	0.158	5.673	0.739	**375308**	48861	25521	74382
24.41	38.37	0.261	5.941	0.767	**393006**	50737	26724	77461
29.84	24.03	0.238	6.057	0.437	**400692**	28917	27247	56165
39.02	9.78	0.158	6.154	1.088	**407114**	71968	27684	99652
27.37	29.55	0.240	6.257	0.578	**413917**	38267	28146	66413
25.65	38.35	0.253	6.286	0.948	**415838**	62690	28277	90967
25.51	38.36	0.254	6.400	0.653	**423398**	43213	28791	72004
28.93	39.20	0.237	6.578	0.593	**435144**	39236	29590	68825
32.89	24.69	0.219	6.824	0.541	**451451**	35802	30699	66501
25.30	49.06	0.254	6.975	0.766	**461424**	50648	31377	82025
43.85	7.75	0.140	7.149	0.390	**472945**	25109	32160	57269
26.99	43.57	0.249	7.589	0.734	**502035**	48534	34138	82672
51.04	7.68	0.119	8.532	0.384	**564440**	24714	38382	63095
29.72	42.81	0.235	11.408	0.896	**754737**	59298	51322	110620
39.84	14.55	0.197	11.906	0.631	**787677**	41747	53562	95309
43.86	15.75	0.158	12.464	0.950	**824553**	62872	56070	118941
42.21	15.74	0.163	12.524	1.103	**828556**	72950	56342	129292
49.15	10.74	0.142	13.283	0.536	**878746**	34483	59755	94238
34.00	34.28	0.221	13.578	1.116	**898265**	73837	61082	134919
39.09	19.47	0.199	14.514	1.004	**960181**	66417	65292	131709
40.15	29.83	0.199	21.556	2.189	**1426029**	144791	96970	241761

A background/noise measurement on the neutron detector yields an average of (0.15 ± 0.1) cps, meaning that all results <0.15 cps (or close with high uncertainty) in Table 2 are to be considered unusable.

Appendix B: Calculations

Back-of-the-envelope calculation of ballpark expected deuterium fluence on target

The D-flux expected on a Ti target during deuterium-loading can be estimated back-of-the-envelope style to give a crude approximation. The main idea is to relate the discharge current to the total number of ions collected by the target. This can be done by noting that the current (coulombs per second) is a direct measure for the amount of electrons that flow to the grid. Noting that field-emission is the driving force of the discharge and electron avalanche does not occur, the total electron flow from PSU towards the grid consists of a) all electrons emitted from field-emission, plus b) all electrons required to neutralize the ions hitting the target. Using the electron-impact mean-free-path it is possible to estimate how many electrons (on average) are needed for 1 ionization. This obtained fraction allows the total current to be split up into an electron-current and an ion-current, where the ion-current is a direct measure for the ion flux. It is assumed all ions are lost to the target, and some rough estimations will be made to determine how many of these ions are fast enough (>2keV) to embed in the titanium.

Starting off with a background pressure of 1 Pa, the mean-free-path of the electrons can be calculated. By the ideal gas law, $n_g = 2.4 * 10^{20}$ m^{-3} for 1 Pa. Since ions of >2keV are of interest, these ions can only be produced by an electron faster than 2 keV. To calculate the mean-free-path of these electrons, the cross-section at 2 keV is used, which is ~ $0.1*10^{-16}$ cm^2. The mean-free-path then becomes ~ 4 meters. By the electrode distance of ~25cm, this means on average one out of every 4/0.25 = 16 electrons that make it past ~2 keV will ionize an ion above 2 keV.

Furthermore, assuming an overall average electron mean free path of ~1 meter, it is assumed that 1 out of every 4 electrons produces an ion globally. Assuming the total current is caused by the combination of field-emitted electrons plus electrons required for neutralizing the ion at the target, it is possible to estimate how many ions strike the grid and how many of these are 'fast'.

Since in this estimate 1 out of 4 electrons (on average) creates an ion, and assuming all ions end up on the target, 1/5th of the total current is responsible for neutralizing said ions as $I = I_{e,field\text{-}emission} + I_{ion} = I_{e,field\text{-}emission} + ¼*I_e$. For ~20 mA = 20 mC/s = $20*10^{-3}*6.24*10^{18} = 1.24*10^{17}$ electrons/s, that means 1/5th of this total is used for neutralizing ions. Noting that 1 out of every 16 electrons faster than 2 keV produces a fast ion, and noting that on average 3 out of every 4 electrons travel past the 2 keV point, a total of $1.24*10^{17}*1/5*1/16*3/4 = 1.17*10^{15}$ ions/s hit the target. For an exposure time of 3600 seconds and a surface area of 6.7 cm^2, the total fluence is then $6*10^{17}$ ions/cm^2, ~10^{18} ions/cm^2.

Maximum momentum exchange in elastic collision

Elastic collisions between particles of unlike mass cannot transfer all kinetic energy, but only a fraction. For an incident particle with E_i colliding on a stationary target particle with $E_t = 0$, the resulting energy after a perfectly head-on collision is given by:

$$E_t = E_i * \frac{4m_t m_i}{(m_t + m_i)^2}$$

For a collision between H and H_2 (or D and D_2), where $m_t = 1$ and $m_i = 2$ (or vice versa), this results in a maximum energy transfer of 88.9%.

Fusion cross-section for D(d,n)

The fusion-cross section as a function of the center-of-mass ion energy was calculated from the parameterization by Bosch et al [18]. The parameterization is:

$$\sigma = \frac{S(E)}{E \exp(B_G/\sqrt{E}}$$

where E is the center-of-mass ion energy in keV, and

$$S(E) = \frac{A1 + E(A2 + E\big(A3 + E(A4 + EA5)\big))}{1 + E(B1 + E\big(B2 + E(B3 + EB4)\big))}$$

The parameters as derived by Bosch are listed in Table 3.

Table 3: Coefficients used for the parameterization [18]

Coefficient	**D(d,n)^{3}He**
B_G ($\sqrt{keV}$)	31.3970
A1	$5.3701*10^4$
A2	$3.3027*10^2$
A3	$-1.2706*10^{-1}$
A4	$2.9327*10^{-5}$
A5	$-2.5151*10^{-9}$
B1, B2, B3 and B4	0

Appendix C: Additional figures

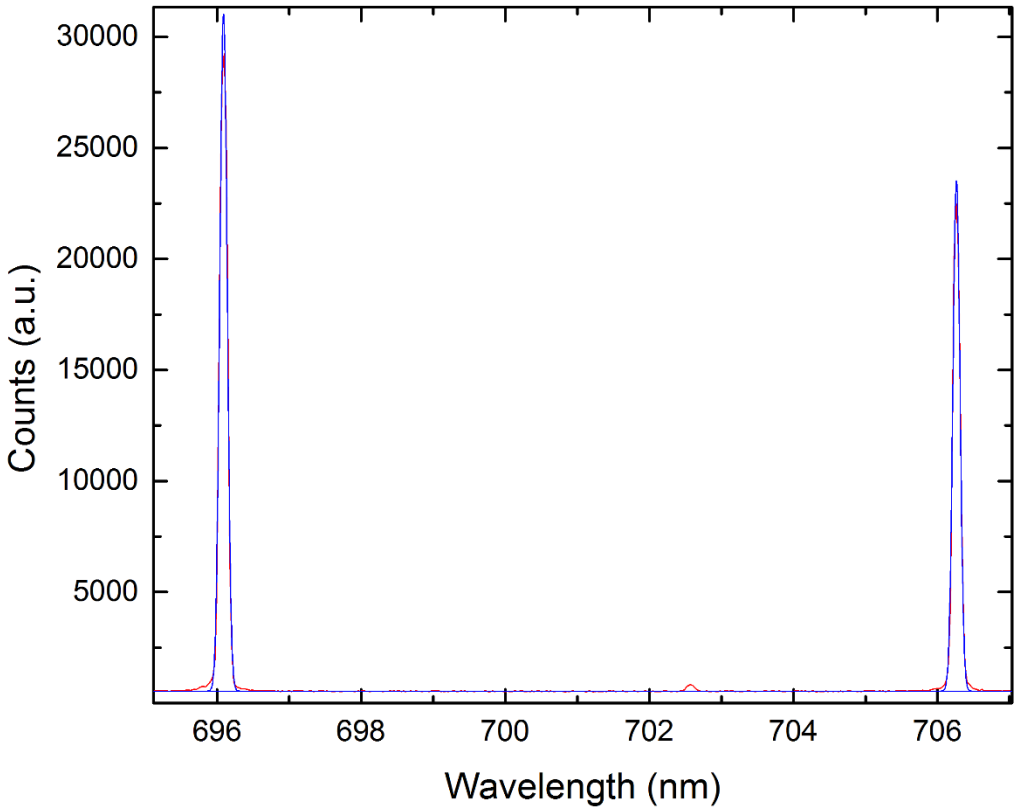

Figure 32: Calibration spectrum (fitted in blue) of an argon lamp, used to determine the instrumental broadening. Recorded FWHM was (0.12 ± 0.01) nm.